Gain-of-function mutations in a member of the Src family kinases cause autoinflammatory bone disease in mice and humans

Koichiro Abe[a,1,2], Allison Cox[b,1], Nobuhiko Takamatsu[c], Gabriel Velez[d,e], Ronald M. Laxer[f], Shirley M. L. Tse[f], Vinit B. Mahajan[d], Alexander G. Bassuk[b], Helmut Fuchs[g], Polly J. Ferguson[b,3], and Martin Hrabe de Angelis[g,h,i,3]

[a]Department of Molecular Life Science, Tokai University School of Medicine, Isehara 259-1193, Kanagawa, Japan; [b]Department of Pediatrics, University of Iowa Carver College of Medicine, Iowa City, Iowa, IA 52242; [c]School of Science, Kitasato University, Sagamihara 252-0373, Kanagawa, Japan; [d]Omics Laboratory, Byers Eye Institute, Stanford University, Palo Alto, CA 94304; [e]Medical Scientist Training Program, University of Iowa Carver College of Medicine, Iowa City, IA 52242; [f]Department of Pediatrics, Hospital for Sick Children, University of Toronto, ON M5G 1X8, Canada; [g]Institute of Experimental Genetics, Helmholtz Zentrum München, 85764 Neuherberg, Germany; [h]Chair of Experimental Genetics, School of Life Science Weihenstephan, Technische Universität München, 85354 Freising, Germany; and [i]German Center for Diabetes Research, 85764 Neuherberg, Germany

Edited by David R. Beier, Seattle Children's Research Institute, Seattle, MA, and accepted by Editorial Board Member Kathryn V. Anderson May 7, 2019 (received for review November 20, 2018)

Autoinflammatory syndromes are characterized by dysregulation of the innate immune response with subsequent episodes of acute spontaneous inflammation. Chronic recurrent multifocal osteomyelitis (CRMO) is an autoinflammatory bone disorder that presents with bone pain and localized swelling. *Ali18* mice, isolated from a mutagenesis screen, exhibit a spontaneous inflammatory paw phenotype that includes sterile osteomyelitis and systemic reduced bone mineral density. To elucidate the molecular basis of the disease, positional cloning of the causative gene for *Ali18* was attempted. Using a candidate gene approach, a missense mutation in the C-terminal region of *Fgr*, a member of Src family tyrosine kinases (SFKs), was identified. For functional confirmation, additional mutations at the N terminus of *Fgr* were introduced in *Ali18* mice by CRISPR/Cas9-mediated genome editing. N-terminal deleterious mutations of *Fgr* abolished the inflammatory phenotype in *Ali18* mice, but in-frame and missense mutations in the same region continue to exhibit the phenotype. The fact that *Fgr* null mutant mice are morphologically normal suggests that the inflammation in this model depends on Fgr products. Furthermore, the levels of C-terminal negative regulatory phosphorylation of Fgr^{Ali18} are distinctly reduced compared with that of wild-type Fgr. In addition, whole-exome sequencing of 99 CRMO patients including 88 trios (proband and parents) identified 13 patients with heterozygous coding sequence variants in *FGR*, including two missense mutant proteins that affect kinase activity. Our results strongly indicate that gain-of-function mutations in *Fgr* are involved in sterile osteomyelitis, and thus targeting SFKs using specific inhibitors may allow for efficient treatment of the disease.

chronic recurrent multifocal osteomyelitis | autoinflammation | mouse model | tyrosine kinase | bone destruction

Autoinflammatory syndromes are disorders of innate immunity characterized by episodes of seemingly unprovoked sterile inflammation without increased autoantibodies or involvement of self-reactive lymphocytes (1). Many autoinflammatory disorders have a monogenic basis, but for most, a combination of genetic and environmental factors contributes to disease susceptibility. Chronic recurrent multifocal osteomyelitis (CRMO), also known as chronic nonbacterial osteomyelitis (CNO), is an autoinflammatory bone disease which presents with bone pain and local swelling due to unifocal, or more often multifocal sites of sterile osteomyelitis (2–5). While the genes for two syndromic forms of CRMO (*LPIN2* and *IL1RN*) are known (6, 7), the genetic etiology for nonsyndromic CNO/CRMO is poorly understood.

A forward genetics approach using animal models is a powerful tool for the molecular dissection of pathogenesis in inflammatory bone diseases (8). Examples include *Pstpip2* (*lupo* and *cmo* mice) (9–11) and *Zap70* (*skg* mice) (12), which were identified and well characterized without human disease data. Further, similar autoinflammatory phenotypes of *Ali5* (13) and *Ali14* (14) mice caused by missense mutations in *phospholipase C gamma* (*Plcg2*) are related to the novel human hereditary disease PLAID (PLCG2-associated antibody deficiency and immune dysregulation) (15, 16). However, most of the intracellular cascades which lead to autoinflammatory diseases are not well known.

The *Ali18* mutant mouse strain was isolated in the Munich ENU mutagenesis project because of paw inflammation (Fig. 1*A*) (17). *Ali18* mice show synovitis, sterile osteomyelitis, and systemic reduced bone mineral density, particularly in trabecular areas of long bones (17). Because these phenotypes are reconstituted by bone marrow transfer and are independent of mature lymphocytes (18), *Ali18* mice are considered a mouse model of autoinflammatory bone disease. Although the *Ali18* locus was mapped to mouse chromosome 4 by standard genetic mapping, complex modifier effects hinder its precise determination (19). In this study, positional candidate cloning identified *Fgr*, a member of Src family kinases, as the causative gene

Significance

Chronic recurrent multifocal osteomyelitis (CRMO) is an autoinflammatory bone disease that presents with bone destruction occurring primarily in children. In a mouse ENU mutagenesis screen, the *Ali18* strain was isolated because of spontaneous inflammation in the joints and bones. Sequencing candidate genes in the *Ali18* critical region identified a missense mutation in the C-terminal regulatory region of the Src family kinase (SFK) member, *Fgr*. Genome editing revealed *Fgr* dependency of the inflammatory phenotype in *Ali18* mice. Further, whole exome sequencing in our CRMO cohort identified two patients with missense mutations in *FGR*. In vitro functional assays confirm altered protein function. This work identifies *FGR* as a CRMO susceptibility gene and suggests that targeting SFKs may be useful in its treatment.

Author contributions: K.A., P.J.F., and M.H.d.A. designed research; K.A., A.C., N.T., G.V., R.M.L., S.M.L.T., H.F., P.J.F., and M.H.d.A. performed research; K.A., A.C., N.T., G.V., R.M.L., S.M.L.T., V.B.M., A.G.B., H.F., and P.J.F. analyzed data; and K.A., A.C., N.T., A.G.B., P.J.F., and M.H.d.A. wrote the paper.

The authors declare no conflict of interest.

This article is a PNAS Direct Submission. D.R.B. is a guest editor invited by the Editorial Board.

[1]K.A. and A.C. contributed equally to this work.

[2]To whom correspondence may be addressed. Email: abeko@is.icc.u-tokai.ac.jp.

[3]P.J.F. and M.H.d.A. contributed equally to this work.

This article contains supporting information online at www.pnas.org/lookup/suppl/doi:10.1073/pnas.1819825116/-/DCSupplemental.

for *Ali18*. Further, two other missense mutations in *FGR* were found in our cohort of patients with CRMO.

Results

***Ali18* Mice, Fine Mapping, and Candidate Resequencing.** By standard genetic mapping, we narrowed down the critical region to ∼3 Mb utilizing recombination between wild-type and heterozygous/homozygous genotypes (Fig. 1*B* and *SI Appendix*, Table S1). In the identified region, we focused on 16 candidate genes using a literature-based search engine, PosMed (20). By sequencing the exonic region of these genes by the Sanger method, we found a mutation, c.1506A > G, in the protein coding region of the Gardner-Rasheed feline sarcoma viral (v-Fgr) oncogene homolog (*Fgr*) gene (21) (Fig. 1*C*). Digestion of PCR products encompassing exon 13 of *Fgr* by Mbo II restriction enzyme, which recognizes the wild-type allele (5′-GAAGA-3′) but not c.1506A > G (5′-GAAGG-3′), produces longer DNA fragments in *Ali18* mice (Fig. 1*D*). Genotype–phenotype correlations revealed that the mutation was not present in unaffected littermates or wild-type controls.

A Member of SFK as the Top Candidate for the Causative Gene. Fgr is a member of the Src family kinases (SFKs), which share the SH2, SH3, and catalytic domains with high homology to other family members (22), and the c.1506A > G mutation causes an amino acid change (p.Asp502Gly) in the terminal end of the catalytic domain (Fig. 1*E*). Alignment of the amino acid sequences of Fgr with those of other SFKs indicates that the 502 aspartic acid is conserved among Src, Fyn, Yes, Lyn, and Lck (Fig. 1*F*). The corresponding amino acid in Hck and Blk is glutamic acid and has a negatively charged side chain as does aspartic acid. The aspartic acid of Fgr is also conserved in humans (Fig. 1*F*, FGR). We searched sequence variants among 36 mouse inbred strains in the "mousepost.be" database (23) and no variants were detected in the *Fgr* locus. The PROVEAN (Protein Variation Effect Analyzer) software (24) predicts that the amino acid substitution is deleterious (score = −6.440; cutoff = −2.5). In addition, we performed whole-genome sequencing by next generation sequencer (NGS) using genomic DNA from *Ali18*/+ and wild-type mice on the same genetic background, and *Fgr* c.1506A > G (IGV_2.3.94, mouse mm10, chr4: 133,000,294, *SI Appendix*, Fig. S1*A*) mutations were found in only *Ali18*/+ DNA as a heterozygous change (NGS reads, A:20 and G:24). Within the *Ali18* critical region, we found three other candidate mutations (IGV_2.3.94, mouse mm10, chr4: 133,543,428; chr4: 133,705,306; chr4: 133,919,389, *SI Appendix*, Fig. S1 *B*–*D*) besides the *Fgr* coding mutation. However, all three mutations are located in noncoding regions.

Deficiency of Fgr Abolishes the Autoinflammatory Phenotype of *Ali18* Mice. To confirm whether the inflammatory phenotype of *Ali18* mice is caused by the *Fgr* coding mutation, we used the prokaryotic antiviral system, CRISPR/Cas9, to induce additional loss-of-function mutations in the N-terminal region of Fgr besides p.Asp502Gly. Because *Fgr* knockout mice show no overt phenotype (25, 26), it is predicted that loss-of-function mutations in *Fgr* do not support the osteomyelitis phenotype in *Ali18* mice. As shown in Fig. 2 *A* and *B*, two pX330 related constructs containing guide RNA around exon 3 of the *Fgr* gene (fgRNA1 and -2) were microinjected into *Ali18*/*Ali18* fertilized eggs. Therefore, all of the *Cas9*-induced mutations are in the *Ali18* haplotype containing the *Fgr* c.1506A > G/p.Asp502Gly mutation (Fig. 2*A*). In the founder (F0) generation, we sequenced the region flanking and including exon 3 which contains the transcriptional initiation site of *Fgr*. All F0 mice (nos. 405, 406, 407, 409, 410, and 411) without mutation around the *Cas9*-targeted PAM sites exhibit the arthritic phenotype (6/6). In contrast, half of the F0 mice harboring mutations around the PAM sites did not show the inflammatory paw phenotype (5/10).

As it is expected that somatic and germ cells of the F0 mice are chimeric with various indel mutations around the PAM, we crossed F0 mice with wild-type C3HeB/FeJ mice to obtain F1 mice without chimerism (Fig. 2*B*). Twelve germline-transmitted lines were established from seven F0 mice with a mutation around PAM (*SI Appendix*, Table S2). Among all 12 lines established, 8 lines, which have deleterious mutations in the *Fgr* coding region, such as frameshift (#404a, #404b, #415a, and #416a) and deletion of translational initiation site (#418) and/or splicing acceptor (#417a and #419), abolish the inflamed paw phenotype of *Ali18* mice (Fig. 2 *C* and *D* and *SI Appendix*, Figs. S2 and S3). In contrast, the other four lines with missense (#408 and #416b), in-frame (#415b), and synonymous (#417b) mutations of *Fgr* exhibit the inflammatory paw phenotype (Fig. 2 *C* and *D* and *SI Appendix*, Figs. S2 and S3 and Table S2).

Interestingly, #408a and #417b F1 mice showed different severity of paw swelling compared with original *Ali18* mice. *Ali18*_#408a (p.Ser25Arg;Asp502Gly) (Fig. 2*D* and *SI Appendix*, Fig. S2*C*) mice show more severely inflamed paws, indicating that combination of the amino acid exchanges enhances paw swelling. The #417b (Fig. 2*C*

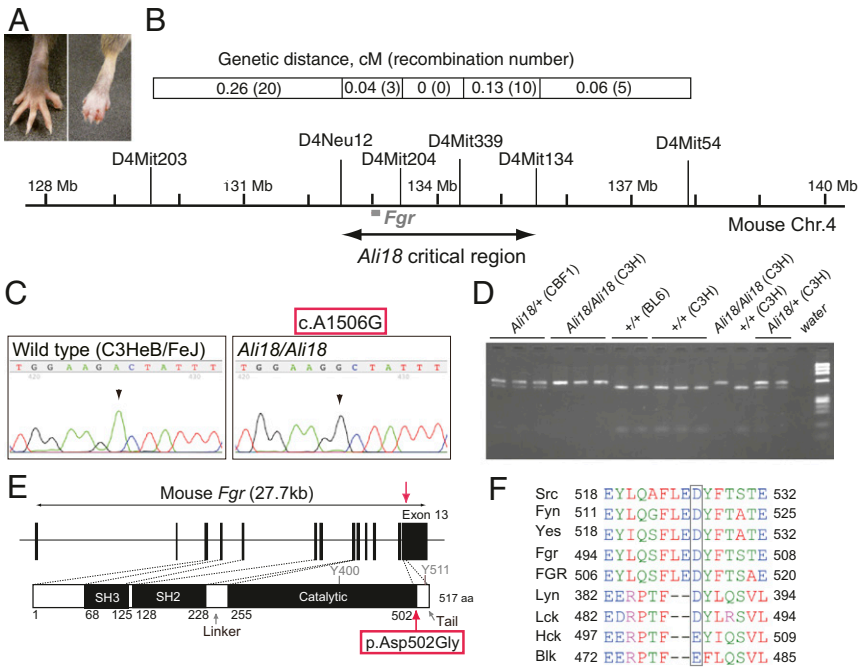

Fig. 1. Positional candidate cloning of the *Ali18* mutation. (*A*) *Ali18*/+ (*Right*) and wild-type C3HeB/FeJ (*Left*) hind paws. *Ali18* mice show reddening and swelling in peripheral paws. (*B*) Genetic map and the critical interval of the *Ali18* locus. The complex modifier effects from the C57BL/6J genetic background prevented further narrowing down of the region. (*C*) By Sanger sequencing of candidate genes in the region, a point mutation (c.1506A > G) in exon 13 of *Fgr*, a member of the SFKs, was detected. (*D*) Mbo II restriction enzyme digestion of PCR products spanning exon 13 correlated to the swollen paw phenotype. Genetic background is described as C3H (C3HeB/FeJ), BL6 (C57BL/6J), and CBF1 (F1 from C3H and BL6 crossing). *Ali18* mice were originally derived from C3H parents. (*E*) Schematic diagram of the p.Asp502Gly (D502G) amino acid change induced by c.1506A > G. Y400 and Y511 indicate the autophosphorylation site and the C-terminal regulatory phosphorylation site, respectively. (*F*) Alignment of Src family tyrosine kinases. Square encompasses the amino acid residues exchanged by the c.1506A > G mutation.

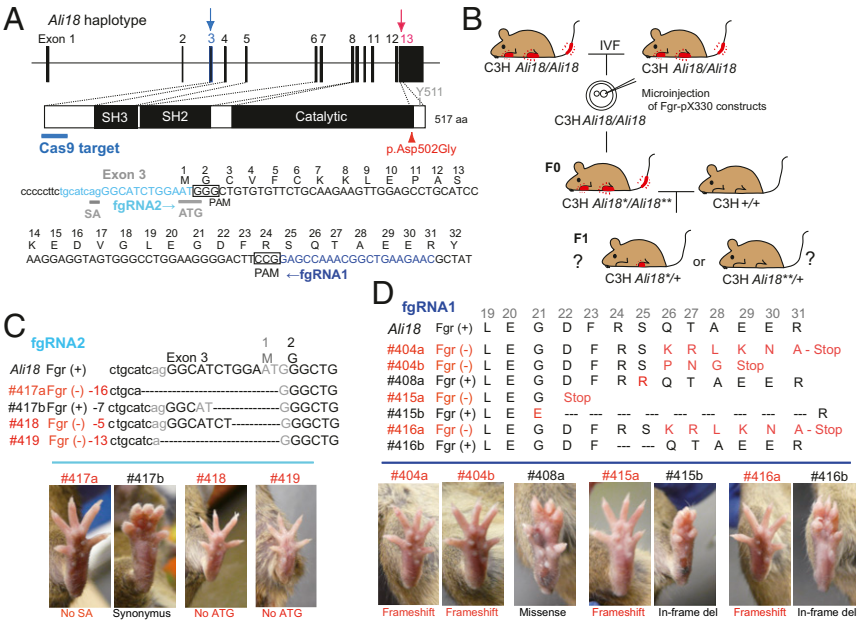

Fig. 2. Disruption of the *Fgr* gene by genome editing alters the autoinflammatory phenotype in *Ali18* mice. (*A*) DNA sequence of guide RNA (fgRNA1 and fgRNA2) and PAM around exon 3 of *Fgr* are indicated. The p.Asp502Gly mutation in exon 13 is also shown. Sanger sequencing of a PCR fragment around exon 3 and genotyping of p.Asp502Gly were done using genomic DNA from F0 and F1 mice. (*B*) Schematic strategy of genome editing in the *Fgr* locus of *Ali18* mice. pX330-based constructs were microinjected into *Ali18/Ali18* oocytes in C3H (C3HeB/FeJ) genetic background from in vitro fertilization. The founder mice (F0) derived from microinjection were bred with wild-type C3H mice to obtain F1 mice. (*C* and *D*) Correlation of *Fgr* genotypes and lower limb morphology of F1 mice. Loss-of-function mutations show no morphological abnormality (red font). In contrast, missense, in-frame deletion, and synonymous mutations exhibit autoinflammatory paws. SA, splice acceptor; ATG, the translational initiation site. See also *SI Appendix*, Table S2 for detail.

and *SI Appendix*, Fig. S2*I*) line, which has an in-frame 5′ UTR deletion with a newly formed ATG codon in *Fgr*, showed swollen paws. However, not all mice of the #417b line showed a swollen paw phenotype (4/9, *SI Appendix*, Table S2 and Fig. S3). It is likely that the newly formed translational initiation site or deletion in the UTR region causes low transcriptional and/or translational efficiency of the Fgr protein. These results strongly support that the *Fgr* p.Asp502Gly mutation is responsible for autoinflammation in *Ali18* mice.

Abnormal C-Terminal Phosphorylation of Fgr^{Ali18} Reveals Gain of Function. To elucidate how the p.Asp502Gly mutation affects Fgr function, we analyzed the tyrosine kinase activities of wild-type and p.Asp502Gly Fgr proteins by standard kinase assay using radioisotope-labeled ATP. Fig. 3*C* shows tyrosine kinase activity of in vitro translated Fgr proteins against affinity purified enolase as a substrate of SFKs. Unlike oncogenic mutations, the kinase activity of p.Asp502Gly Fgr was not dramatically changed. These results were also supported by Western blot analysis using antiphosphotyrosine in *Ali18/Ali18* organs and Fgr p.Asp502Gly expressing cultured cells (Fig. 3 *A* and *B*). We then focused on efficiency of the C-terminal phosphorylation, because p.Asp502Gly is located close to this phosphorylation site. SFKs are normally inactive with the C-terminal phosphorylation by C-terminal Src kinase (Csk, another member of SFKs). To detect the C-terminal phosphorylation, a kinase-ablation mutation (KD, kinase dead) is necessary to avoid autophosphorylation of Src (27). Therefore, we used affinity purified Fgr protein with a p.Lys279Met (K279M) kinase dead mutation (Fgr_{KD}, WT) and Fgr_{KD} with the p.Asp502Gly mutation ($Fgr_{KD}^{Asp502Gly}$, mut) as substrates for kinase assays by Csk. As shown in Fig. 3*D*, specifically phosphorylated products were detected in the samples containing Csk without autophosphorylation. Further, the efficiency of phosphorylation of Fgr_{KD} (WT) by Csk is approximately two times more than that of $Fgr_{KD}^{Asp502Gly}$ (mut) (relative activity ratio: 0.472 ± 0.072). The decrease of C-terminal phosphorylation indicates that $Fgr^{Asp502Gly}$ is more active than wild-type protein. These results strongly suggest that p.Asp502Gly is a gain-of-function mutation of the Fgr tyrosine kinase.

***FGR* Coding Variants Were Detected in Autoinflammatory Bone Disease Patients.** As part of a human CRMO genetic study, whole-exome sequencing by NGS was performed on 99 affected individuals and their family members. The families included 88 family trios (affected and both unaffected parents) and 11 dyads (affected and one unaffected parent). *FGR* variants from affected subjects were queried, and 11 rare exonic variants in total were identified in 13 probands (*SI Appendix*, Table S3). These include two missense variants, p.Arg118Trp and p.Pro525Ser (Fig. 4*H*). For the patient with the p.Arg118Trp mutation, radiographs show osteolytic lesion with sclerosis and periosteal reaction in distal femur (Fig. 4 *A* and *B*) which demonstrated abnormal signal intensity and enhancement on postcontrast MRI compatible with CRMO; an additional MRI shows abnormal inflammation detected in the sacroiliac joint by short-tau inversion recovery (STIR) (Fig. 4*C*).

Genomic DNA from the patient and parents was validated by Sanger sequencing, and the chromatograms indicate a de novo mutation in the child with the p.Arg118Trp *FGR* mutation (Fig. 4*D*). A p.Pro525Ser variation is detected in another child for which DNA from only one parent was available, so it is not known if the variant is inherited or de novo. MRI abnormalities in the fibula of the child are shown in Fig. 4 *E*–*G*. Both variants are rare (*SI Appendix*, Table S3); the p.Arg118Trp (rs774209795) and p.Pro525Ser (rs143850913) variants have minor allele frequencies of 1.2×10^{-5} and 3.5×10^{-4}, respectively, according to gnomAD (28). The PROVEAN software predicts that both amino acid substitutions are deleterious; the score of p.Arg118Trp is −5.015 (cutoff = −2.5); the score of p.Pro525Ser is −2.716 (cutoff = −2.5) and the other predictors including SIFT, Polyphen2, and CADD also predict pathogenicity (*SI Appendix*, Table S5). There were no mutations in the known CRMO susceptibility genes including *FBLIM1*, *IL1RN*, *LIPIN2*, or *PSTPIP2* in these two patients (*SI Appendix*, Table S3). However, the same missense variant in *FBLIM1* was found in two patients with FGR splice or synonymous mutations, and a missense mutation in *LIPIN2* was detected in a patient with an *FGR* 5′ UTR mutation (*SI Appendix*, Tables S3 and S4). All three variants are *in trans* with the coding *FGR* variant based on parental genotypes. The *FBLIM1* variant identified in two probands induces a p.Gly311Arg amino acid change and the *LPIN2* variant induces a p.Cys874Phe change.

To elucidate functional abnormality of the variants found in CRMO patients, kinase assay experiments were performed using affinity purified mutant FGR proteins and enolase (Fig. 4 *I* and *J*). The p.Arg118Trp FGR protein (RW, Fig. 4*H*) show decreased phosphorylation compared with that of wild-type protein (WT) (relative activity ratio: 0.39 ± 0.12, $P < 0.0001$, *t* test, Fig. 4 *I and J*). As shown in *SI Appendix*, Figs. S4 and S5, the structural model of p.Arg118Trp may lead to disruption of SH3-kinase linker interaction which destabilizes the protein functions (see also *SI Appendix*, *Results and Discussion*). In contrast, p.Pro525Ser (PS, Fig. 4*H*) may inhibit the closed-inactive formation of FGR as predicted by the structural model (*SI Appendix*, Fig. S6). Actually, the kinase assay

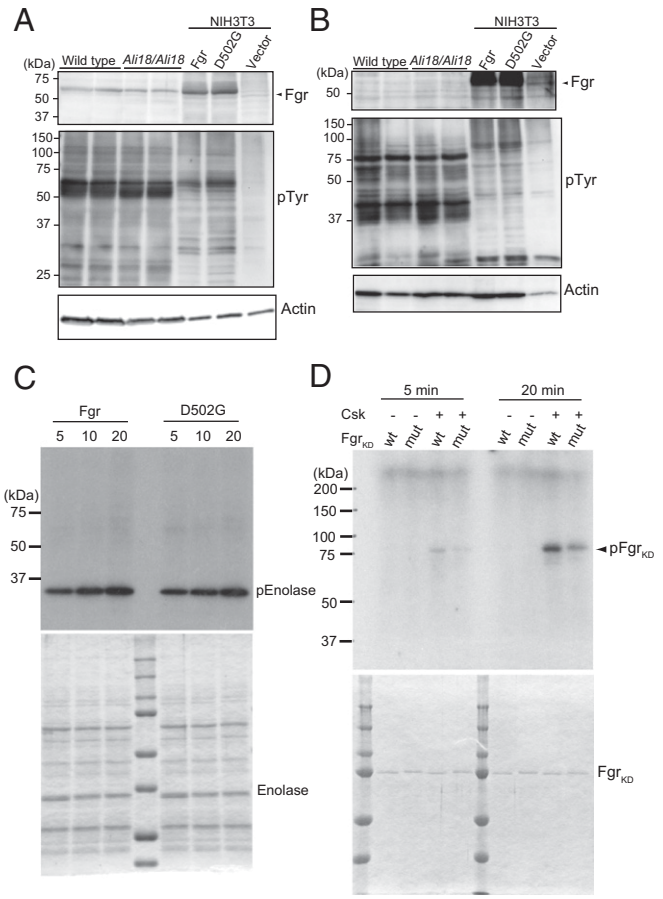

Fig. 3. Western blot analysis, tyrosine kinase assays, and phosphorylation of Fgr by C-terminal Src kinase (Csk). Cell lysate of spleen (*A*) and bone marrow cells (*B*) from wild-type and *Ali18/Ali18* mice were used for Western blotting. As control experiments, transformants of wild-type and p.Asp502Gly (D502G) Fgr expression constructs in murine embryo-derived cultured fibroblast, NIH 3T3, cells were used. Empty vector was transfected as negative control. Anti-Fgr (*Upper*), anti-phosphotyrosine (*Middle*), and anti-actin (*Lower*, loading control) were used. No overt changes in Fgr protein levels of *Ali18/Ali18* spleen (relative ratio: 0.900 ± 0.256, $P = 0.538$, *t* test) and NIH 3T3 cells (relative ratio: 0.982 ± 0.139, $P = 0.833$, *t* test) were detected. (*C*) In vitro translated wild-type and p.Asp502Gly Fgr proteins were used for kinase assay experiments. Recombinant enolase protein was used as SFK-specific substrate (*Lower*, loading control). No activity changes were detected in different reaction time. (*D*) The C-terminal phosphorylation of KD Fgr by Csk was measured. Fgr KD with p.Asp502Gly showed five and two times less phosphorylation levels in 5- and 20-min reaction time, respectively. The proteins used for kinase assays were fractionated by SDS/PAGE and stained by Coomassie Brilliant Blue. Experiments were independently triplicated.

experiments of PS show increased levels of phosphorylation compared with WT (relative activity ratio: 1.20 ± 0.05, $P = 0.015$, *t* test, Fig. 4 *I and J*). Unlike the *Ali18* mutation, the decreased levels of C-terminal phosphorylation of kinase dead RW and PS by Csk were not observed (Fig. 4*K*). However, both murine p.Arg106Trp (corresponding to PS) and p.Arg106Trp;p.Asp502Gly Fgr constructs showed an ∼10% decrease in C-terminal phosphorylation by Csk compared with the wild-type and p.Asp502Gly Fgr constructs, respectively (*SI Appendix*, Fig. S7).

Discussion

In this study, we identified *Fgr* as the causative gene for inflammatory disease in the *Ali18* mutant mice by positional candidate cloning despite complex modifier effects from the genetic background. Further genetic studies by genome editing confirmed that multiple null alleles of *Fgr* disrupt the inflammatory paw phenotype in *Ali18* mice. Previously, it was shown that the *Ali18* phenotype occurs independently of the adaptive immune system (disease occurs in *Ali18;Rag1*$^{-/-}$ mice that lack B and T cells); further, granulocytes are increased in peripheral blood of *Ali18* mice (18). Fgr is predominantly expressed in myeloid

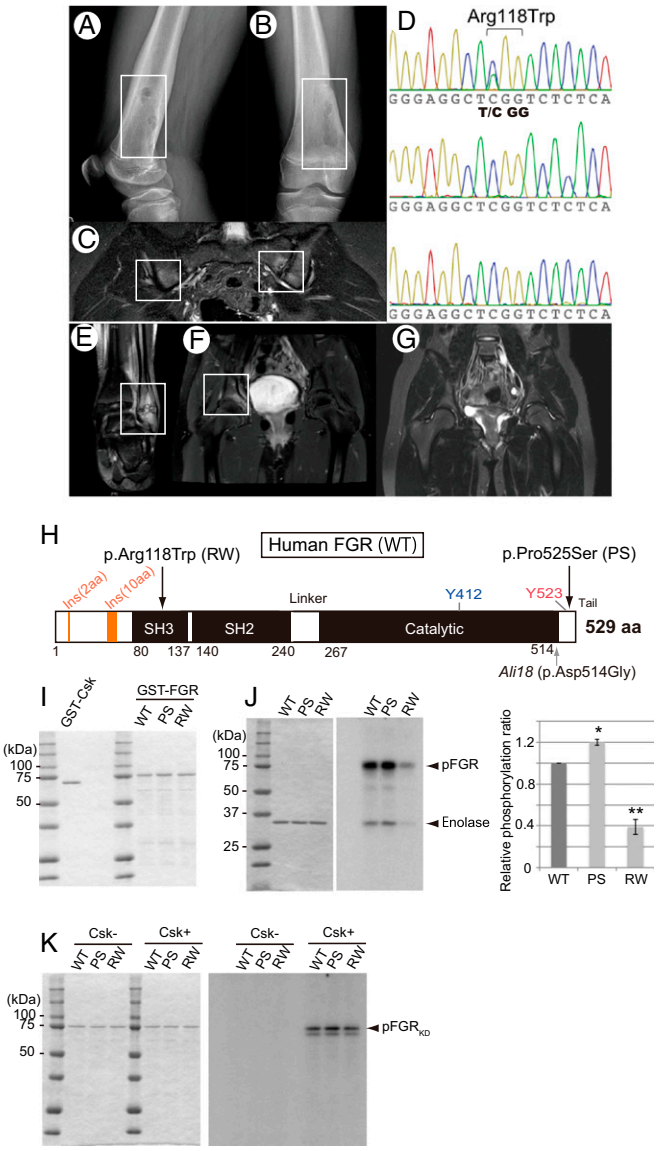

Fig. 4. Missense mutations of *FGR* in CRMO and phosphorylation assays. (*A* and *B*) Radiograph of case 1 (p.Arg118Trp). Osteolytic lesions with sclerosis and periosteal elevation of the right distal femur are shown. (*C*) MRI of case 1. Increased STIR signal intensity on the iliac and sacral sides of the left sacroiliac joints is shown. (*D*) Sanger sequencing chromatogram of p.Arg118Trp in the proband (*Top*), father (*Middle*), and mother (*Bottom*). Proband harbors a de novo C > T mutation, which induces a p.Arg118Trp amino acid change in *FGR*. (*E–G*) MRI of case 2 (p.Pro525Ser). Abnormalities included increased signal intensity on STIR images in the left distal fibula (*E*) and the pelvis at the right acetabulum (*F*). (*G*) Repeat MRI 9 mo after naproxen therapy showing improvement in the left acetabular lesion. (*H*) Schematic diagram of amino acid substitution from the *FGR* mutations found in human CRMO (*Top* arrows) and the mouse *Ali18* mutation (*Lower* arrow). (*I*) SDS/PAGE of affinity purified Csk and FGR used in kinase assays. (*J*) Kinase activity of FGR with CRMO variants. (*J*, *Left*) SDS/PAGE of affinity purified substrate, enolase, used in each assay. (*J*, *Right*) Phosphorylation intensity of enolase and FGR indicate enzyme activity. (*K*) Phosphorylation of FGR_{KD} with CRMO variants by Csk. (*Left*) SDS/PAGE of affinity purified FGR_{KD} of human CRMO variants as substrate used in each assay. (*Right*) FGR_{KD} proteins were phosphorylated by Csk in equal intensity. Experiments were independently triplicated.

lineage cells such as granulocytes, monocytes, and dendritic cells (29). This expression pattern fits the cell populations implicated in the autoinflammatory phenotype of *Ali18* mice. Because Fgr plays an important role in mast cell activation (30, 31) and neutrophil adhesion (29), these cell types are likely contributing independently, or in combination, to autoinflammation in *Ali18* mice and is the subject of ongoing research.

In SFKs, the C-terminal region is important for inactivation of tyrosine kinase activity; therefore defects in the C-terminal region cause constitutive activation, which leads to cancerization (32, 33). Csk is another member of SFKs and specifically phosphorylates a C-terminal tyrosine of SFKs (34). Without C-terminal phosphorylation by Csk, SFKs cannot form a folded inactive conformation. For this phosphorylation, it is known that docking between the C-terminal region of SFKs and Csk is necessary (27). In our results, $Fgr^{Asp502Gly}$ was less phosphorylated than wild-type Fgr by Csk. The corresponding amino acid substitution in Src (p.Asp518Ala) also shows decreased phosphorylation of the C-terminal region (27). Thus, it strongly suggests that constitutive activation of Fgr leads to the inflammatory phenotypes of *Ali18* mice.

In the *cmo* (*chronic multifocal osteomyelitis*) mouse model, the proinflammatory cytokine IL1-β mediates autoinflammation but does not require the Nlrp3 inflammasome (35). In Fgr^{Ali18} mice, IL1β is not up-regulated in peripheral blood (18). Although Fgr is not known to activate the inflammasome directly, NEK7 serine-threonine kinase and two tyrosine kinases, Btk and Syk, control inflammasome activation by phosphorylation (36). Thus, the phosphorylation network is important for regulation of inflammasome activation in myeloid cells. Recently, it was reported that phosphorylation of CBL ubiquitin ligase at Y371 by SFKs negatively controls NLRP3 inflammasome activation (37). Further, Cbl ubiquitinates Fgr directly for its activation (38). Thus, gain of function of Fgr may lead to the activation loop of Fgr-Cbl which suppresses the NLRP3 inflammasome. These suggest that autoinflammation caused by Fgr activation occurs independent of Nlrp3 inflammasome activation.

In the cohort of patients with CRMO, we found two *FGR* coding variants, p.Arg118Trp and p.Pro525Ser, which are located in the SH3 domain and C-terminal tail, respectively. Since decreased C-terminal phosphorylation by Csk was not observed using human *FGR* constructs, it is likely that mouse and human mutations have different functional properties. Increased kinase activation was observed in p.Pro525Ser FGR. Pro525 is the only hydrophobic amino acid in the C terminus of FGR. In the inactive form of Src, the C-terminal region is bound to two hydrophobic pockets of the protein surface in the SH2 domain (39, 40). The substitution of the substitution of Pro525 for hydrophilic Ser could be repellent to the surface of the hydrophobic binding pocket. Because the surface region is conserved between Src and Fgr (39), p.Pro525Ser FGR probably leads to instability of the inactive form. Thus, the active form of FGR could dominate the signaling cascade in the patient. In contrast, the role of p.Arg118Trp in CRMO pathogenesis remains difficult to define. The murine equivalent p.Arg106Trp mutation showed a decrease in phosphorylation versus wild-type murine Fgr, yet in vitro functional studies of p.Arg118Trp in human, constructs showed decreased kinase activity. Since human FGR has additional amino acid residues at the N terminus (amino acid residues 14–15 and 49–58; Fig. 4*H*) compared with murine Fgr, we hypothesize that these structural differences in FGR influence C-terminal phosphorylation. As described in *Results*, *Ali18_#*408a (p.Ser25Arg;Asp502Gly) mice exhibited more severe inflammatory phenotypes; this genetic model supports the importance of C- and N-terminal interactions in Fgr function. While the de novo status of the p.Arg118Trp mutation strongly supports its pathogenicity, in the absence of additional human CRMO cases with the same mutation, *Fgr* p.Arg106Trp mutant mice or *FGR* p.Arg118Trp knockin mice are needed to better determine the role of this mutation in sterile bone inflammation.

The genetic etiology of most sporadic CRMO cases is not yet known and it is likely that variants at multiple loci, in addition to environmental factors, both contribute together to disease development. We queried sequence data from the 13 CRMO probands with *FGR* coding variants for additional protein coding changes in the other CRMO candidate genes. A p.Gly311Arg change in *FBLIM1* was identified in two probands and a p.Cys874Phe change in *LPIN2* was identified in one proband. The *FBLIM1* variant is not rare, with a minor allele frequency of 0.0195 in gnomAD and is in the FERMT2-binding domain, not the filamin-binding domain as was the variant previously reported (41). Phosphorylation of FERMT2 by Src facilitates interaction of FERMT2 with FBLIM1, and this complex then is recruited to focal adhesions as part of integrin-mediated cellular signaling (42). The concurrent and compound heterozygous status of both *FGR* and *FBLIM1* variants in CRMO probands is supportive of genetic interactions between the two genes and future experiments will verify if variants in FGR or FBLIM1 found in CRMO patients disrupt this feedback loop. Regarding the *LPIN2* missense variant, to date there is no established interaction between LIPIN2 and FGR.

We experimentally showed that inactivation of *Fgr* by genome editing abolished autoinflammatory bone and joint disease in *Fgr* p.Asp502Gly mutant *Ali18* mice. This suggests targeting FGR function would be of potential therapeutic benefit in humans with autoinflammatory phenotypes. Tyrosine kinase inhibitors effective against SFK, including PP1, PP2, and dasatinib (43, 44), are therapeutic candidates. In particular, dasatinib relieves bone pain in animal models of cancer-induced bone pain (45). Such small molecule inhibitors may be effective on other members of SFKs, by targeting the ATP binding domain; however, this increases the likelihood of side effects. Recently, however, the FGR-specific inhibitor, TL02-59, has been identified as a suppressor of acute myelogenous leukemia cell growth (46). Testing these therapies in *Ali18* mice will help determine the effectiveness of SFK inhibitors as a potential therapeutic target for the treatment of CRMO and other inflammatory diseases.

In conclusion, we identified the tyrosine kinase FGR as a functional intracellular signaling molecule involved in the pathogenesis of autoinflammatory bone diseases. Dysregulation of active–inactive conformational changes in FGR protein leads to osteomyelitis in mice and humans. Thus, trial and development of SFK inhibitors using the animal model will provide insights into the potential for therapeutic options in the treatment of human CRMO.

Methods

Mice. The *Ali18* strain (C3HeB/FeJ-Mhdaali18) was established in the Munich mouse ENU mutagenesis project (47), and its character and maintenance have been described previously (17, 19). For genotyping of the *Fgr* locus of *Ali18* mice, see *SI Appendix, Methods*. All animal care and experimental protocols using mice were conducted in accordance with the Tokai University Institutional Animal Care and Use Committee, and all animal research was approved by this committee before the experiments.

Positional Candidate Cloning. Standard genetic mapping was used to narrow down the critical region (17, 19). In the region, we used a literature-based search engine, PosMed (20), to select candidate genes. Because bone marrow cells from *Ali18* mice could reconstitute the inflammatory phenotype of *Ali18* mice in irradiated wild-type mice (18), we used "bone marrow" as a keyword for search by PosMed. Sixteen genes were selected, and PCR primer pairs spanning the exonic region were designed by ExonPrimer (https://ihg.helmholtz-muenchen.de). The PCR products from wild-type and *Ali18*/*Ali18* templates were then sequenced by standard Sanger sequencing.

Genome Editing of *Ali18* Mice. A standard DNA microinjection method into *Ali18*/*Ali18* fertilized eggs was performed (48) using pX330-based constructs described in *SI Appendix, Methods*. To obtain *Ali18*/*Ali18* fertilized eggs, in vitro fertilization with *Ali18*/*Ali18* oocyte and sperm was done. The CRISPR/Cas9-mediated mutations of F0 and F1 mice were confirmed by Sanger sequencing. We only used F0 mice (*Ali18*/*Ali18*) with newly introduced mutations in exon 3 of *Fgr* for further mating with C3HeB/FeJ mice to obtain F1 mice (*Ali18*/+).

Western Blotting. Western blotting was done by a standard procedure as previously described (49). Antibodies used in this study were as follows: anti-Fgr (M60) (sc-50338, Santa Cruz Biotechnology, Inc.), anti-phosphotyrosine (06–427, Upstate), and anti-actin (A5471, Sigma). For protein preparation from tissues and cultured cells, see *SI Appendix, Methods*.

Protein Purification for Kinase Assays. The in vitro transcription/translation system was used to synthesize mouse Fgr protein (TNT Quick Systems, Promega). GST-Csk (mouse), GST-Fgr_{KD} (mouse), and GST-FGR and GST-FGR_{KD} (human) were expressed in *Escherichia coli* BL21(DE3), purified by glutathione

GENETICS

Sepharose 4B (GE Healthcare), and stored in 50 mM Tris·HCl, pH 8.0, at −80 °C. Purity of the purified proteins was examined by SDS-polyacrylamide gel electrophoresis and Coomassie Brilliant Blue (CBB) staining. Protein concentrations were determined by using a Pierce BCA Protein Assay Kit (Thermo Scientific). For the phosphorylation assay procedures, see *SI Appendix, Methods*.

Clinical Samples and Exome Sequencing. All human research was approved by the University of Iowa Institutional Review Board. Written informed consent was obtained from all clinical study participants and written parental or guardian consent was obtained, because all participants were under the age of 18. Use of clinical samples, whole-exome sequencing, and data analysis is described previously in detail (41), although more recent Agilent exome platforms (V5 and V6+UTR) were used for 8/99 samples (V5) and 79/99 (V6+UTR) samples.

ACKNOWLEDGMENTS. We thank Kumiko Ishikawa, Maya Tanigawa, Miyu Hirano, Miyuki Kitabayashi, Kumiko Sugizaki, and Hideo Tsukamoto for excellent technical assistance. We are also thankful to Sanae Ogiwara, Ayaka Nakamura, and Yutaka Ishikawa for mouse embryo manipulation. This work was supported in part by grants from Japan Society for the Promotion of Science (JSPS 19500370 and 22500392), Takeda Science Foundation, and Research Foundation of Ituu to K.A., German Federal Ministry of Education and Research (Infrafrontier Grant 01KX1012 to M.H.d.A.), the National Institutes of Health (National Institute of Arthritis, Musculoskeletal and Skin R01AR059703 to P.J.F. and A.G.B.). V.B.M. and A.G.B. are supported by NIH Grants (R01EY026682, R01EY024665, R01EY025225, R01EY024698, and R21A050437), the Doris Duke Charitable Foundation Grant 2013103, and Research to Prevent Blindness New York, NY. G.V. is supported by NIH Grants (F30EYE027986 and T32GM997337).

1. S. L. Masters, A. Simon, I. Aksentijevich, D. L. Kastner, Horror autoinflammaticus: The molecular pathophysiology of autoinflammatory disease (*). *Annu. Rev. Immunol.* **27**, 621–668 (2009).
2. A. Jansson *et al*., Classification of non-bacterial osteitis: Retrospective study of clinical, immunological and genetic aspects in 89 patients. *Rheumatology (Oxford)* **46**, 154–160 (2007).
3. P. J. Ferguson, M. Sandu, Current understanding of the pathogenesis and management of chronic recurrent multifocal osteomyelitis. *Curr. Rheumatol. Rep.* **14**, 130–141 (2012).
4. S. R. Hofmann *et al*., Chronic recurrent multifocal osteomyelitis (CRMO): Presentation, pathogenesis, and treatment. *Curr. Osteoporos. Rep.* **15**, 542–554 (2017).
5. M. R. Roderick, E. S. Sen, A. V. Ramanan, Chronic recurrent multifocal osteomyelitis in children and adults: Current understanding and areas for development. *Rheumatology (Oxford)* **57**, 41–48 (2018).
6. P. J. Ferguson *et al*., Homozygous mutations in LPIN2 are responsible for the syndrome of chronic recurrent multifocal osteomyelitis and congenital dyserythropoietic anaemia (Majeed syndrome). *J. Med. Genet.* **42**, 551–557 (2005).
7. I. Aksentijevich *et al*., An autoinflammatory disease with deficiency of the interleukin-1-receptor antagonist. *N. Engl. J. Med.* **360**, 2426–2437 (2009).
8. K. Abe, P. Yu, Positional cloning in mice and its use for molecular dissection of inflammatory arthritis. *Curr. Pharm. Biotechnol.* **10**, 252–260 (2009).
9. J. Grosse *et al*., Mutation of mouse Mayp/Pstpip2 causes a macrophage autoinflammatory disease. *Blood* **107**, 3350–3358 (2006).
10. L. Byrd, M. Grossmann, M. Potter, G. L. Shen-Ong, Chronic multifocal osteomyelitis, a new recessive mutation on chromosome 18 of the mouse. *Genomics* **11**, 794–798 (1991).
11. P. J. Ferguson *et al*., A missense mutation in pstpip2 is associated with the murine autoinflammatory disorder chronic multifocal osteomyelitis. *Bone* **38**, 41–47 (2006).
12. N. Sakaguchi *et al*., Altered thymic T-cell selection due to a mutation of the ZAP-70 gene causes autoimmune arthritis in mice. *Nature* **426**, 454–460 (2003).
13. P. Yu *et al*., Autoimmunity and inflammation due to a gain-of-function mutation in phospholipase C gamma 2 that specifically increases external Ca2+ entry. *Immunity* **22**, 451–465 (2005).
14. K. Abe *et al*., A novel N-ethyl-N-nitrosourea-induced mutation in phospholipase Cγ2 causes inflammatory arthritis, metabolic defects, and male infertility in vitro in a murine model. *Arthritis Rheum.* **63**, 1301–1311 (2011).
15. M. J. Ombrello *et al*., Cold urticaria, immunodeficiency, and autoimmunity related to PLCG2 deletions. *N. Engl. J. Med.* **366**, 330–338 (2012).
16. Q. Zhou *et al*., A hypermorphic missense mutation in PLCG2, encoding phospholipase Cγ2, causes a dominantly inherited autoinflammatory disease with immunodeficiency. *Am. J. Hum. Genet.* **91**, 713–720 (2012).
17. K. Abe, H. Fuchs, T. Lisse, W. Hans, M. Hrabe de Angelis, New ENU-induced semidominant mutation, Ali18, causes inflammatory arthritis, dermatitis, and osteoporosis in the mouse. *Mamm. Genome* **17**, 915–926 (2006).
18. K. Abe *et al*., Novel lymphocyte-independent mechanisms to initiate inflammatory arthritis via bone marrow-derived cells of Ali18 mutant mice. *Rheumatology (Oxford)* **47**, 292–300 (2008).
19. K. Abe *et al*., Genome-wide search for genes that modulate inflammatory arthritis caused by Ali18 mutation in mice. *Mamm. Genome* **20**, 152–161 (2009).
20. Y. Yoshida *et al*., PosMed (Positional Medline): Prioritizing genes with an artificial neural network comprising medical documents to accelerate positional cloning. *Nucleic Acids Res.* **37**, W147–W152 (2009).
21. G. Naharro *et al*., Molecular cloning of integrated Gardner-Rasheed feline sarcoma virus: Genetic structure of its cell-derived sequence differs from that of other tyrosine kinase-coding onc genes. *J. Virol.* **47**, 611–619 (1983).
22. M. T. Brown, J. A. Cooper, Regulation, substrates and functions of src. *Biochim. Biophys. Acta* **1287**, 121–149 (1996).
23. S. Timmermans, M. Van Montagu, C. Libert, Complete overview of protein-inactivating sequence variations in 36 sequenced mouse inbred strains. *Proc. Natl. Acad. Sci. U.S.A.* **114**, 9158–9163 (2017).
24. Y. Choi, G. E. Sims, S. Murphy, J. R. Miller, A. P. Chan, Predicting the functional effect of amino acid substitutions and indels. *PLoS One* **7**, e46688 (2012).
25. C. A. Lowell, P. Soriano, H. E. Varmus, Functional overlap in the src gene family: Inactivation of hck and fgr impairs natural immunity. *Genes Dev.* **8**, 387–398 (1994).
26. C. A. Lowell, P. Soriano, Knockouts of Src-family kinases: Stiff bones, wimpy T cells, and bad memories. *Genes Dev.* **10**, 1845–1857 (1996).
27. S. Lee, M. K. Ayrapetov, D. J. Kemble, K. Parang, G. Sun, Docking-based substrate recognition by the catalytic domain of a protein tyrosine kinase, C-terminal Src kinase (Csk). *J. Biol. Chem.* **281**, 8183–8189 (2006).
28. M. Lek *et al*.; Exome Aggregation Consortium Analysis of protein-coding genetic variation in 60,706 humans. *Nature* **536**, 285–291 (2016).
29. C. A. Lowell, Src-family kinases: Rheostats of immune cell signaling. *Mol. Immunol.* **41**, 631–643 (2004).
30. J. H. Lee *et al*., The Src family kinase Fgr is critical for activation of mast cells and IgE-mediated anaphylaxis in mice. *J. Immunol.* **187**, 1807–1815 (2011).
31. R. Suzuki *et al*., Molecular editing of cellular responses by the high-affinity receptor for IgE. *Science* **343**, 1021–1025 (2014).
32. S. A. Courtneidge, Activation of the pp60c-src kinase by middle T antigen binding or by dephosphorylation. *EMBO J.* **4**, 1471–1477 (1985).
33. J. A. Cooper, K. L. Gould, C. A. Cartwright, T. Hunter, Tyr527 is phosphorylated in pp60c-src: Implications for regulation. *Science* **231**, 1431–1434 (1986).
34. M. Okada, Regulation of the SRC family kinases by Csk. *Int. J. Biol. Sci.* **8**, 1385–1397 (2012).
35. S. L. Cassel *et al*., Inflammasome-independent IL-1β mediates autoinflammatory disease in Pstpip2-deficient mice. *Proc. Natl. Acad. Sci. U.S.A.* **111**, 1072–1077 (2014).
36. T. Gong, W. Jiang, R. Zhou, Control of inflammasome activation by phosphorylation. *Trends Biochem. Sci.* **43**, 685–699 (2018).
37. I. C. Chung *et al*., Src-family kinase-Cbl axis negatively regulates NLRP3 inflammasome activation. *Cell Death Dis.* **9**, 1109 (2018).
38. F. Melander, T. Andersson, K. Dib, Fgr but not Syk tyrosine kinase is a target for beta 2 integrin-induced c-Cbl-mediated ubiquitination in adherent human neutrophils. *Biochem. J.* **370**, 687–694 (2003).
39. G. Waksman *et al*., Crystal structure of the phosphotyrosine recognition domain SH2 of v-src complexed with tyrosine-phosphorylated peptides. *Nature* **358**, 646–653 (1992).
40. G. Waksman, S. E. Shoelson, N. Pant, D. Cowburn, J. Kuriyan, Binding of a high affinity phosphotyrosyl peptide to the Src SH2 domain: Crystal structures of the complexed and peptide-free forms. *Cell* **72**, 779–790 (1993).
41. A. J. Cox *et al*., Recessive coding and regulatory mutations in FBLIM1 underlie the pathogenesis of chronic recurrent multifocal osteomyelitis (CRMO). *PLoS One* **12**, e0169687 (2017).
42. Z. Liu *et al*., Kindlin-2 phosphorylation by Src at Y193 enhances Src activity and is involved in Migfilin recruitment to the focal adhesions. *FEBS Lett.* **589**, 2001–2010 (2015).
43. J. H. Hanke *et al*., Discovery of a novel, potent, and Src family-selective tyrosine kinase inhibitor. Study of Lck- and FynT-dependent T cell activation. *J. Biol. Chem.* **271**, 695–701 (1996).
44. T. O'Hare *et al*., Inhibition of wild-type and mutant Bcr-Abl by AP23464, a potent ATP-based oncogenic protein kinase inhibitor: Implications for CML. *Blood* **104**, 2532–2539 (2004).
45. C. K. Appel *et al*., The Src family kinase inhibitor dasatinib delays pain-related behaviour and conserves bone in a rat model of cancer-induced bone pain. *Sci. Rep.* **7**, 4792 (2017).
46. M. C. Weir *et al*., Selective inhibition of the myeloid Src-family kinase Fgr potently suppresses AML cell growth in vitro and in vivo. *ACS Chem. Biol.* **13**, 1551–1559 (2018).
47. M. Hrabe de Angelis *et al*., Genome-wide, large-scale production of mutant mice by ENU mutagenesis. *Nat. Genet.* **25**, 444–447 (2000).
48. M. Hogan, R. Beddingtom, F. Constantini, E. Lacy, *Manipulating the Mouse Embryo* (Cold Spring Harbor Laboratory Press, New York, ed. 2, 1994).
49. K. Abe *et al*., Novel ENU-induced mutation in Tbx6 causes dominant spondylocostal dysostosis-like vertebral malformations in the rat. *PLoS One* **10**, e0130231 (2015).

PNAS
www.pnas.org

Supplementary Information for

Gain-of-Function Mutations in a Member of the Src Family Kinases Cause Autoinflammatory Bone Disease in Mice and Humans

Koichiro Abe[a,1,*], Allison Cox[b,1], Nobuhiko Takamatsu[c], Gabriel Velez[d,e], Ronald M. Laxer[f], Shirley M.L. Tse[f], Vinit B. Mahajan[d], Alexander G. Bassuk[b], Helmut Fuchs[g], Polly J. Ferguson[b,2] & Martin Hrabě de Angelis[g,h,i,2]

Koichiro Abe
Email: abeko@is.icc.u-tokai.ac.jp

This PDF file includes:

Supplementary text
Figs. S1 to S7
Tables S1 to S4
References for SI reference citations

www.pnas.org/cgi/doi/10.1073/pnas.1819825116

Supplementary Information

Main Text

Results and Discussion

Structural modeling of mutated FGR proteins. We have used structural modeling to help determine the pathogenicity of gene mutations (1-3), and did so for the FGR mutants. Crystal structures for SRC, both in its active and inactive form, have been solved (4). We generated three-dimensional models of FGR using these structures as templates (*SI Appendix,* Fig. S4 and S6).

The *de novo* Arg118Trp mutation removes a positive charge near the distal loop of the SH3 domain, a domain involved in mediating peptide bonding and protein-protein interactions (5) (*SI Appendix,* Fig. S4*A*). We ran all-atom molecular dynamics simulations of the wild-type and p.Arg188Trp SH3 domains using the AMBER14 force field for 100-ns each (*SI Appendix,* Fig. S5). Superimposition of the final structures

obtained during this 100-ns simulation showed that the p.Arg118Trp disrupts a hydrogen bonding interaction with the neighboring Thr125 residue (*SI Appendix,* Fig. S4*C*). In the SRC inactive state the SH3-SH2 domain forms a hinge that is in the closed conformation (4). During activation, the SH3 and SH2 domain unlatch from the C-terminal portion of the protein, making Tyr416 open for phosphorylation (*SI Appendix,* Fig. S4*A*). Disruption of this interaction may destabilize the protein, either enhancing autophosphorylation or preventing C-terminal phosphorylation by Csk.

The Pro525Ser mutation is located on the C-terminal tail of the FGR structure. The C-terminal tail is a critical regulatory region of the protein, and thus, its composition is highly conserved (*SI Appendix,* Fig. S6*B*). Phosphorylation of Tyr523 by Csk inactivates the enzyme by keeping it in its closed conformation. This prevents ulterior phosphorylation of Tyr412, which is important to form its open active confirmation (4). In the closed conformation, the C-terminal region binds to two hydrophobic pockets of the SH2 domain (6). Phosphorylated Tyr523 binds to the N-terminal hydrophobic pocket specifically, and the following three amino acid residues are important for this binding (6). The surface of the pocket is neutral in charge by hydrophobic residues

positioned in SH2. Thus, it is expected that the Pro525Ser mutation prevent the hydrophobic interactions within the pocket, leading to instability to form the closed confirmation (*SI Appendix,* Fig. S6*A*). Thus, it is suggested that the Pro525Ser mutation causes abnormal activation–inactivation cycles of FGR protein. This could lead to constitutive activation of FGR as observed in the *Ali18* mouse.

Methods

Whole genome sequencing (WGS) by next generation sequencer (NGS).

Genomic DNA for WGS was extracted from *Ali18/+* and wild type kidney using QIAGEN genome tip by manufactures protocol. Briefly, the frozen kidneys were crushed by Cryo-Press (MICROTEC CO., LTD, Chiba, Japan), and then crushed powder was used for column separation. The quality of genomic DNA was assessed by Victor 3 fluorometry and gel electrophoresis, and the library construction and HiSeq NGS were ordered to Macrogen Japan (http://www.macrogen-japan.co.jp/). The sequence data were analyzed by IGV (http://software.broadinstitute.org).

Genotyping of *Ali18* mice. The MIT microsatellite markers used for genetic mapping are described previously (7, 8). The D4Neu12 and D4Neu6 markers were originally made using microsatellite sequences detected in the critical region of Mouse Genome sequence database; D4Neu12-L, 5'-CTGGGTCTTCAGAGCTACGTC; D4Neu12-

R, 5’-GATCTGAGGACTGTGGGGAT; D4Neu6-L, 5’-CTCCTGATTCCATTGCAGTG; D4Neu6-R, 5’-CTATGTAGTCAGAGCTGTCCTGG.

After sequence detection of the p.Asp502Gly mutation, we continue to use the PCR primer pair of the exon of the *Fgr* gene for *Ali18* genotyping. Genomic PCR was performed using the following oligonucleotides spanning exon12 to exon13 of the *Fgr* gene: Fgr_ex10-11L, 5’-TTAATCCAGCAGTTCCCAGG and Fgr_ex10-11R, 5’-GGGATTGGCAAGAGCAAG. The PCR products were directly digested with the Mbo II restriction enzyme (NEB). MboII specifically recognizes wild type (5’-GAAGA-3’) but not *Ali18* (5’-GAAGG-3’) sequences in the PCR products.

For genotyping of F0 and F1 mice produced by genome editing, we sequenced PCR products of exon 3 of the *Fgr* gene around the translational initiation site using the following oligonucleotides: Fgr_ex1L, 5’-TAGTGGTACACCAGCCAGGG, and Fgr_ex1R, 5’-CGTTGAGCTAGAGAATAGAGCTG. In addition, PCR-based genotyping of F0 mice was performed for the $Fgr^{Asp502Gly}$ mutation described above.

Histology and bone inflammation scoring. Hind paws were sectioned by standard histological procedure with formic acid decalcification as described previously (9). Bone inflammation was scored for each bone of feet (talus, calcaneus, navicular bone, cuneiform bone, metatarsal bone, and phalanx) according to the percentage of the bone marrow space containing inflammatory cells; 0 (no inflammation), 1 (< 25%), 2 (25-75%), and 3 (>75%). The bone inflammation scores were then averaged for each F1 animals.

Protein preparation from tissues and transfection. Protein samples were prepared from tissues of *Ali18/+* and *Ali18/Ali18* mice. Tissues were once frozen, and then used for making tissue powder by Cryo-Press (MICROTEC CO., LTD, Chiba, Japan). Bone marrow was flushed from femur, and put through nylon mesh; the cells were centrifuged and used for protein preparation. Protein extract was dissolved with buffer containing 1x complete protease inhibitor cocktail (Roche) and 1x phosphatase inhibitor cocktail (Nacalai tesque, Japan), and sonicated for 10 minutes. Plasmid DNA described in *SI Appendix*, Methods, was transfected into the NIH3T3 cells using the

FuGENE reagent (Roche diagnostics). After 72 hours from transfection, cells were harvested for protein preparation as described above.

Protein phosphorylation assays. Phosphorylation of Eno1 by Fgr, FGR or their mutants was analyzed according to Bagheri-Yarmand *et al.* (10) with slight modifications. One and half μg of GST-Eno1 with 4 μl of *in vitro* transcription/translation reaction of Flag-Fgr or its mutant, or 50 ng of GST-FGR or its mutants were suspended in 15 μl of kinase buffer [20 mM Hepes, pH 7.6, 10 mM MgCl2, 1 mM beta-glycerolphosphate, 2.5 mM NaF, 1 mM Na3VO4, 1 mM DTT] containing 20 μM ATP and 5 μCi of [gamma-^{32}P]ATP. After 5 or 20 min at 30°C, the reaction was terminated by the addition of 2.5x Laemlli sample buffer, and applied to 10% SDS-polyacrylamide gel. GST-Eno1 was visualized by CBB staining, and then, the gel was subjected to autoradiography.

Phosphorylation of Fgr_{KD} or FGR_{KD} by Csk was analyzed as follows. One μg of GST-Fgr_{KD} or GST-FGR_{KD} alone or with 10 ng of Csk were suspended in 15 μl of kinase buffer

[20 mM Hepes, pH 7.6, 10 mM MgCl2, 1 mM beta-glycerophosphate, 2.5 mM NaF, 1 mM Na3VO4, 1 mM DTT] containing 20 μM ATP and 5 μCi of [γ-^{32}P]ATP. After 20 min at 30°C, the reaction was terminated by the addition of 2.5x Laemlli sample buffer and applied to 8.5% SDS-polyacrylamide gel. GST-Fgr_{KD} and GST-FGR_{KD} were visualized by CBB staining, and then, the gel was subjected to autoradiography.

Plasmids. For overexpression experiments in cultured cells, the constructs were made in house. Briefly, bone and bone marrow cDNA were synthesized using RNA from whole femur of wild-type C3HeB/FeJ and *Ali18/Ali18* mice, and full coding *Fgr* cDNA was amplified using a pair of PCR primers (Fgr_rt2L, 5'-GTCTGTGGGGGCATCTGG and Fgr_rt2R, 5'-GGGATTGGCTGATGCCCAGT). The PCR products were cloned into the pTARGET vector (Promega). The insert *Fgr* coding sequences of wild type (w21) and p.Asp502Gly (A14R5) were confirmed by Sanger sequencing.

For construction of the expression plasmids of mouse *Csk*, *Fgr* (wt) and *Fgr* (mut, p.Asp502Gly), the corresponding entire coding regions were amplified by PCR using the following oligonucleotide: CSK-SpeIATG_L1, 5'-

TTCAACTAGTATGTCFGGCAATACAGGCCG; Csk-TGAHindIII, 5'-TTAAAGCTTTCACAGGTGCAGCTCATGGGT; Fgr_SpeI-L1, 5'-TTCAACTAGTAGGGCTGTGTGTTCTGCA; FgrTGA_HindII-R2, 5'-TTAAAGCTTCTATGTCTGGTCTCCAGGCTG. PCR products were digested with Spe I and Hind III, and then cloned into the corresponding sites of pET49b (Novagen) using the TAKARA Ligation Kit. The insert *Fgr* sequence with no undesired (Ftw) and p.Asp502Gly mutations (FTA) and the *Csk* with no undesired mutations (2-2-2) were confirmed by Sanger sequencing. To repress autophosphorylation of *Fgr*, a p.Lys279Met (K279M) mutation was introduced using the following oligonucleotides: Fgr-K279M_L1, 5'-CAGTGATGACGCTGAAGCCGGGCA; Fgr-K279M_R1, 5'-CAGCGTCATCACTGCCACCTTTGTGC. The insert sequence with the desired mutation was confirmed by Sanger sequencing (Ftw_KM1 and FTA_KM4).

For kinase assays using human *FGR* mutations, the ORF clone (OHu28536D) was purchased from Genscript Japan. The coding region of *FGR* was cloned into pGEX4T2 (GE Healthcare). The p.P525S and p.R118W mutations were introduced using the following oligonucleotides: hFGR3'-XhoI_R2-, 5'-

GCCGCTCGAGTCTATGTCTGATCCCCGGACTGG; FGR_R118W_L1, 5'-GGAGGCTTGGTCTCTCAGCTC; FGR_R118W_R1, 5'-TGACCACCCTCCGAACCAGAGA. For phosphorylation by Csk, a kinase dead mutation was introduced into above constructs using the following oligonucleotides: FGR_K291M_L1, 5'-GGTGATGACGCTGAAGCCGGGCA and FGR_K291M_R1, 5'-GTGATTCCACCGCACTACTGCGAC.

For construction of the expression plasmid for mouse enolase 1 from amino acid 3 to 92, PCR product of the corresponding region was cloned into the *Eco*RI and *Xho*I sites of pGEX-4T-2 using the following oligonucleotides: mEno1-147FE (*Eco*RI), 5'-ATTCGCCATGTGAATTCTCAGGAT-3'; mEno1-447RX (*Xho*I), 5'-GTCCATCTCGAGCATCAGCTTGT-3'.

In genome editing of *Ali18* mice, to introduce various mutations around exon 3 of the *Fgr* gene in *Ali18* mice, we used the CRISPR/Cas9 system using the pX330-U6-Chimeric_BB-CBh-hSPCas9 vector(11)(https:adgene.org/42230). Two guided RNA sequences, f-gRNA1 (f-gRNA1_L: 5'-CACCGTTCTTCAGCCGTTTGGCTC and f-gRNA1_R: 5'- AAACGAGCCAAACGGCTGAAGAAC) and f-gRNA2 (f-gRNA2_L: 5'-

CACCTGCATCAGGGCATCTGGAAT, and f-gRNA2_R:

AAACATTCCAGATGCCCTGATGCA), were cloned into the Bbs I site of the pX330 vector according to the Addgene's CRISPR guide (https://www.addgene.org/crispr/guide/).

Structural modeling and molecular dynamics simulations. The three-dimensional structure of the active FGR (residues 77-529) was modeled off the crystal structure of the human tyrosine kinase c-SRC (PDB:1FMK (12); 74% sequence identity) using MODELLER 9.14 (13). The resultant model superimposed well with the template and had an RSMD of 0.2 A over 410 Ca atoms. The inactive FGR structure was modeled using the inactive c-SRC (PDB:1Y57) (4) structure as a template. The resultant model had an RSMD of 0.2A over 358 Ca atoms. *In silico* mutagenesis was performed in PyMOL (Schrödinger Corporation). Charges and hydrogen atoms were added to the wild-type and mutant FGR model using PDB2PQR (14). Electrostatic potentials were calculated using APBS (15). Protein and solvent dielectric constants were set to 2.0 and 78.0, respectively. PyMOL generated all structural figures (Schrödinger Corporation).

We performed all-atom molecular dynamics (MD) simulations of wild-type and p.Arg118Trp FGR SH3 domain models using YASARA 15.7.25 software package (16). The system was then subjected to 250 ps restrained equilibration simulation in the NVT ensemble. Temperature was set to 298K and the system was solvated in water with 0.9% NaCl and a pH of 7.4. The AMBER14 (17) all-atom force field was then run for 100 ns with trajectory conformations saved every 250 ps. Analysis were performed using the YASARA macros md analyze.mcr and md analyzers.mcr.

Figure S1

A


Mouse (mm10)
chr4
chr4:133,000,243-133,000,344
Go
qA1 qA2 qA3 qA4 qA5 qB1 qB2 qB3 qC1 qC3 qC4 qC5 qC6 qC7 qD1 qD2.2 qD3 qE1 qE2
A133000294G
133,000,260 bp
133,000,280 bp
133,000,300 bp
133,000,320 bp
133,000,340 bp
0781-2_Alil8_sort.bam Coverage
0781-2_Alil8_sort.bam
0736-1_AGA3_sort.bam Coverag
0736-1_AGA3_sort.bam
Sequence
Refseq genes
Fgr
6 tracks loaded
chr4:133,000,339
282M of 640M

Figure S1

B


IGV
File Genomes View Tracks Regions Tools GenomeSpace Help
Mouse (mm10)
chr4
chr4:133,543,370-133,543,494
Go
A133543428G
133,543,380 bp
133,543,400 bp
133,543,420 bp
133,543,440 bp
133,543,460 bp
133,543,480 bp
0781-2_AliI8_sort.bam Coverage
0781-2_AliI8_sort.bam
0736-1_AGA3_sort.bam Coverag
0736-1_AGA3_sort.bam
Sequence
Refseq genes
6 tracks loaded
chr4:133,543,413
286M of 311M

Figure S1

C


IGV
File Genomes View Tracks Regions Tools GenomeSpace Help
Mouse (mm10)
chr4
chr4:133,705,245-133,705,369
Go
A133705306G
126 bp
133,705,260 bp
133,705,280 bp
133,705,300 bp
133,705,320 bp
133,705,340 bp
133,705,360 bp
0781-2_AliI8_sort.bam Coverage
0781-2_AliI8_sort.bam
0736-1_AGA3_sort.bam Coverag
0736-1_AGA3_sort.bam
Sequence
Refseq genes
6 tracks loaded
chr4:133,705,332
595M of 812M

Figure S1

D

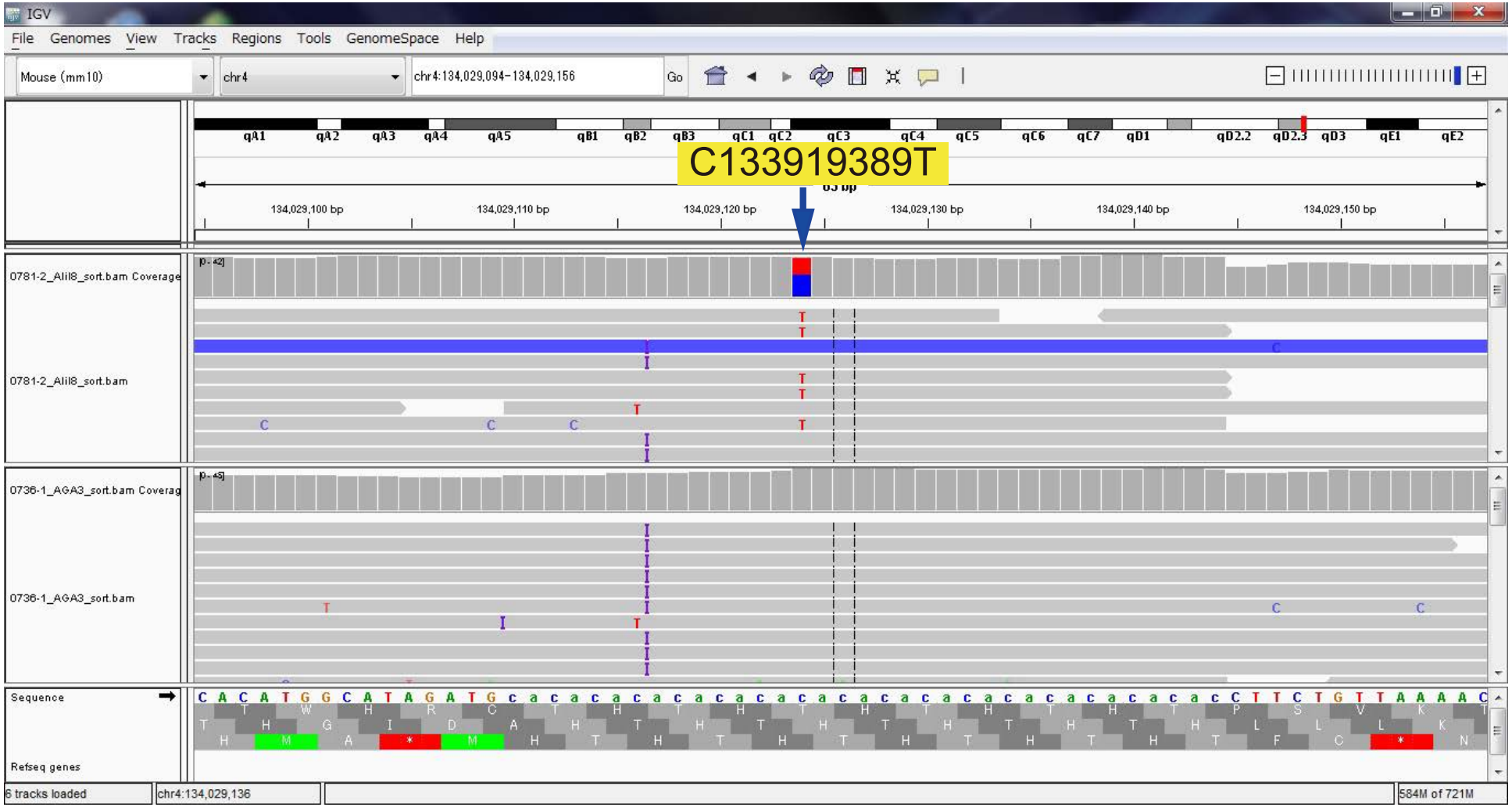
IGV
File Genomes View Tracks Regions Tools GenomeSpace Help
Mouse (mm10)
chr4
chr4:134,029,094-134,029,156
Go
C133919389T
134,029,100 bp
134,029,110 bp
134,029,120 bp
134,029,130 bp
134,029,140 bp
134,029,150 bp
0781-2_Alil8_sort.bam Coverage
0781-2_Alil8_sort.bam
0736-1_AGA3_sort.bam Coverag
0736-1_AGA3_sort.bam
Sequence
Refseq genes
6 tracks loaded
chr4:134,029,136
584M of 721M

Figure S2

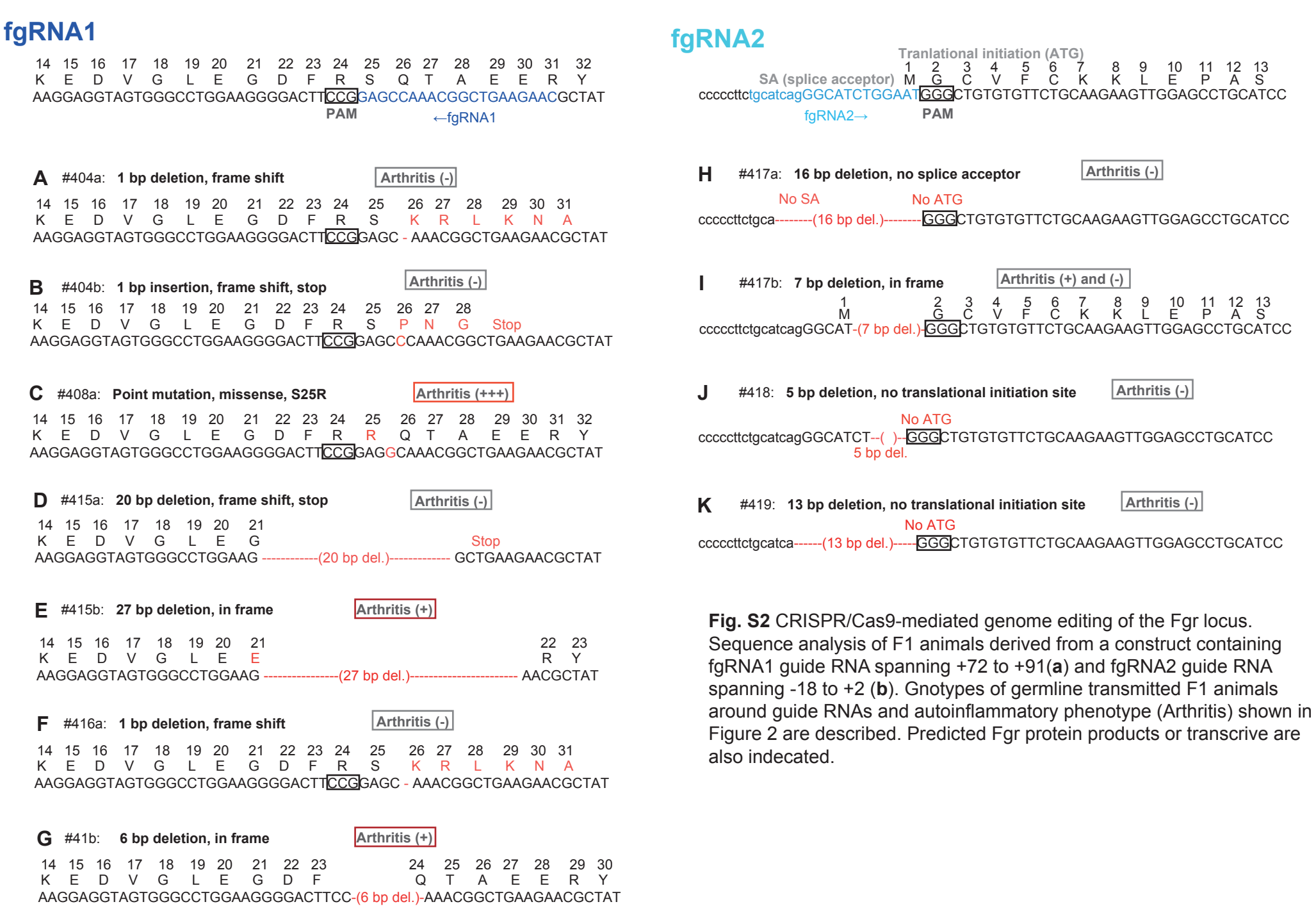

Fig. S2 CRISPR/Cas9-mediated genome editing of the Fgr locus. Sequence analysis of F1 animals derived from a construct containing fgRNA1 guide RNA spanning +72 to +91(**a**) and fgRNA2 guide RNA spanning -18 to +2 (**b**). Gnotypes of germline transmitted F1 animals around guide RNAs and autoinflammatory phenotype (Arthritis) shown in Figure 2 are described. Predicted Fgr protein products or transcrive are also indecated.

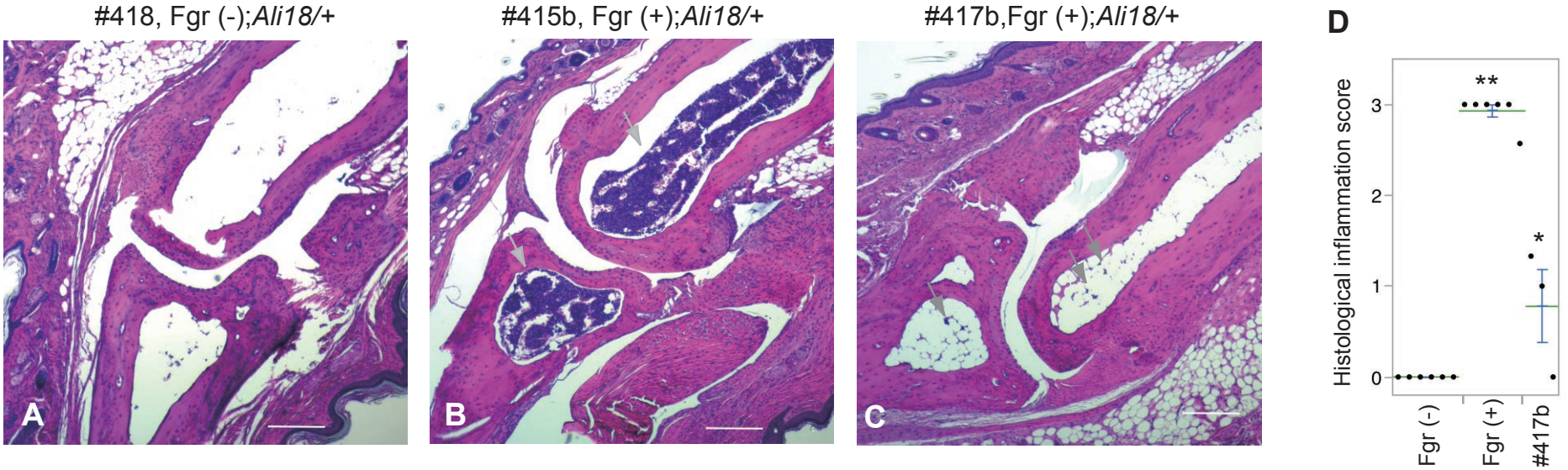

Fig. S3 Histological analysis of peripheral paws of F1 mice with genetic modification by CRISPR/*Cas9*-mediated genome editing of the *Fgr* locus. (A) Hematoxylin and eosin (HE) stained sections of the joint between talus and navicular bone from #418 strain F1 mice are indicated. The #418 strain has a deleterious mutation of *Fgr*. Other strains with the same mutation type are grouped as Fgr (-). (B) HE stained sections of the joint between talus and navicular bone from #415 F1 mice are indicated. The #415 has a missense (in flame) mutation of *Fgr*. Other strains with in flame mutation type are grouped as Fgr (+). Inflammtory cells in bone marrow are indicated by arrows. (C) HE stained sections of the joint between talus and navicular bone from #417 F1 mice. #417 has deletion in exon 3 but resuled in intact Fgr. #417 F1 mice show a partial inflammatory paw phenotype. (D) Histological scoring for severity of bone inflammation was performed on peripheral paws of F1 mice. Fgr (+) (n = 6), Fgr(-) (n = 6), and #417b (n = 3) were used. Average bar (x axis) and SE bar (y axis) are shown. *: $P < 0.005$; **: $P < 0.0001$ by paird *t*-tests.

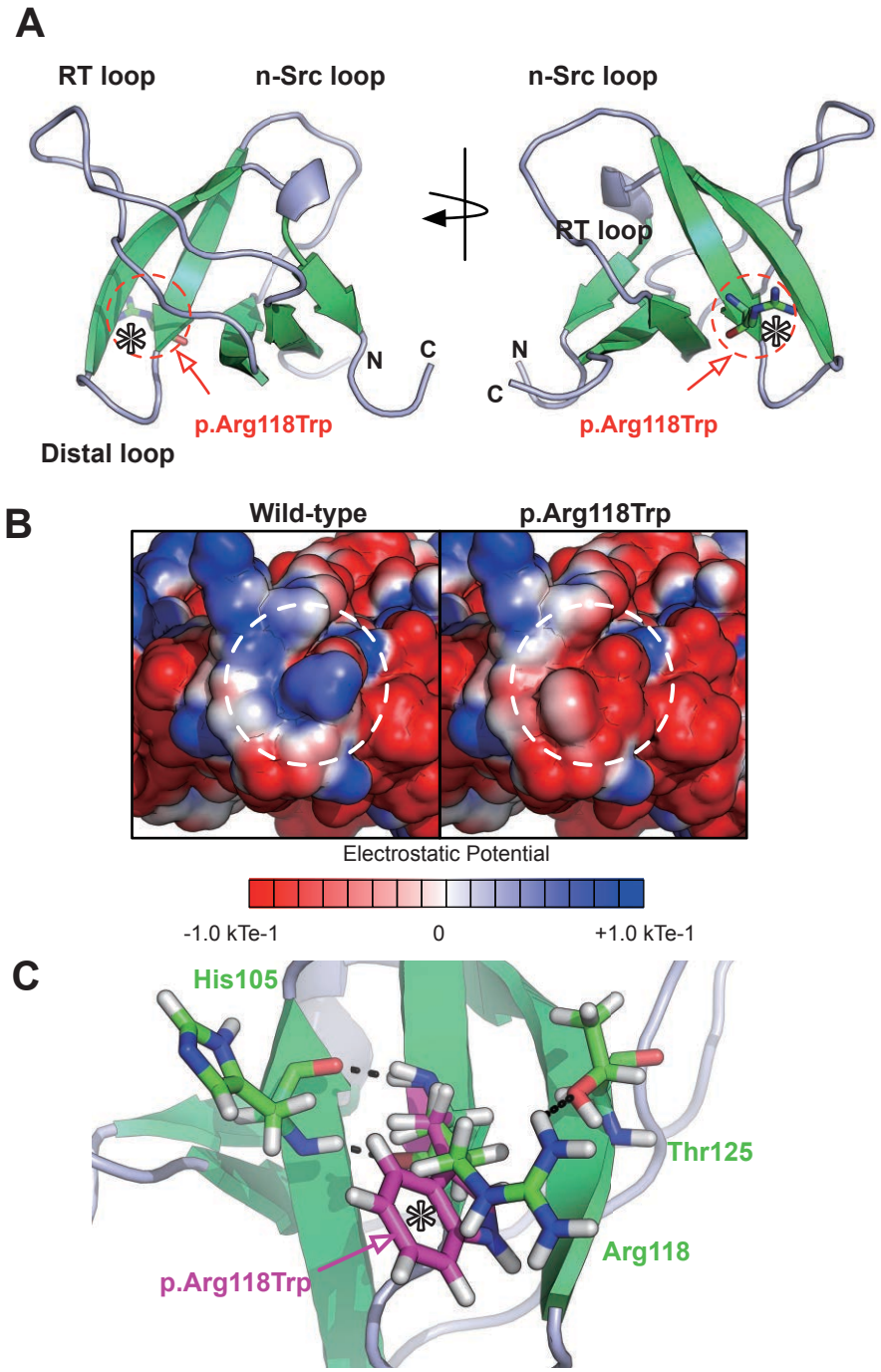

Fig. S4. Predicted mechanism of the human FGR p.Arg118Trp mutation.

(**A**) Structural model of the FGR SH3 domain generated using C-SRC as a template (PDB: 1FMK). The p.Arg118Trp mutation is located in a beta strand near the distal loop of the SH3 domain. (**B**) Wild-type and p.Arg118Trp electrostatic potentials were analyzed using APBS. The p.Arg118Trp mutation leads to a loss of positive charge. (**C**) Superimposition of the final structures obtained during a 100-ns simulation. The p.Arg118Trp disrupts a hydrogen bonding interaction with the neighboring Thr125 residue. Asterisk indecates amino acid substitution.

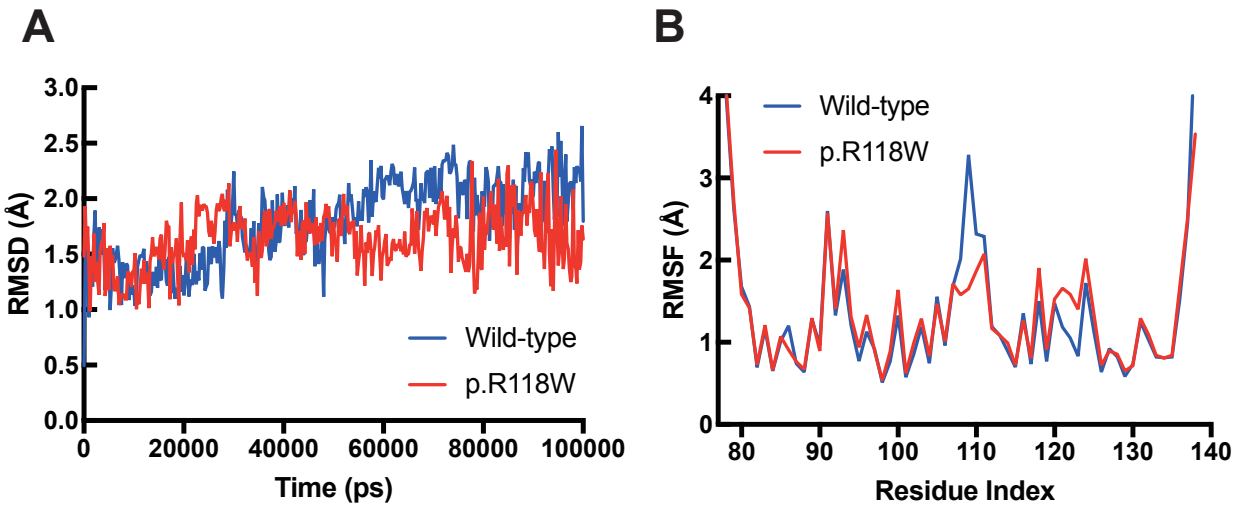

Fig. S5 Molecular dynamics simulations of the wild-type and p.Arg118Trp FGR SH3 domain. (**A**) Both wild-type and p.Arg118Trp SH3 domain models were analyzed using all-atom molecular dynamics (MD) simulations (100-ns each). Root mean square deviation (RMSD) values of the FGR SH3 domain backbone atoms were calculated relative to the initial minimized structure throughout the simulation. Both the wild-type and p.Arg118Trp FGR reached equilibrium at around 30-ns of simulation. (**B**) Further analysis of root mean square fluctuation (RMSF) versus the protein residue for the wild-type and p.Arg118Trp FGR SH3 domains is illustrated. Both the wild-type and mutant SH3 domains possess the similar RMSF distributions.

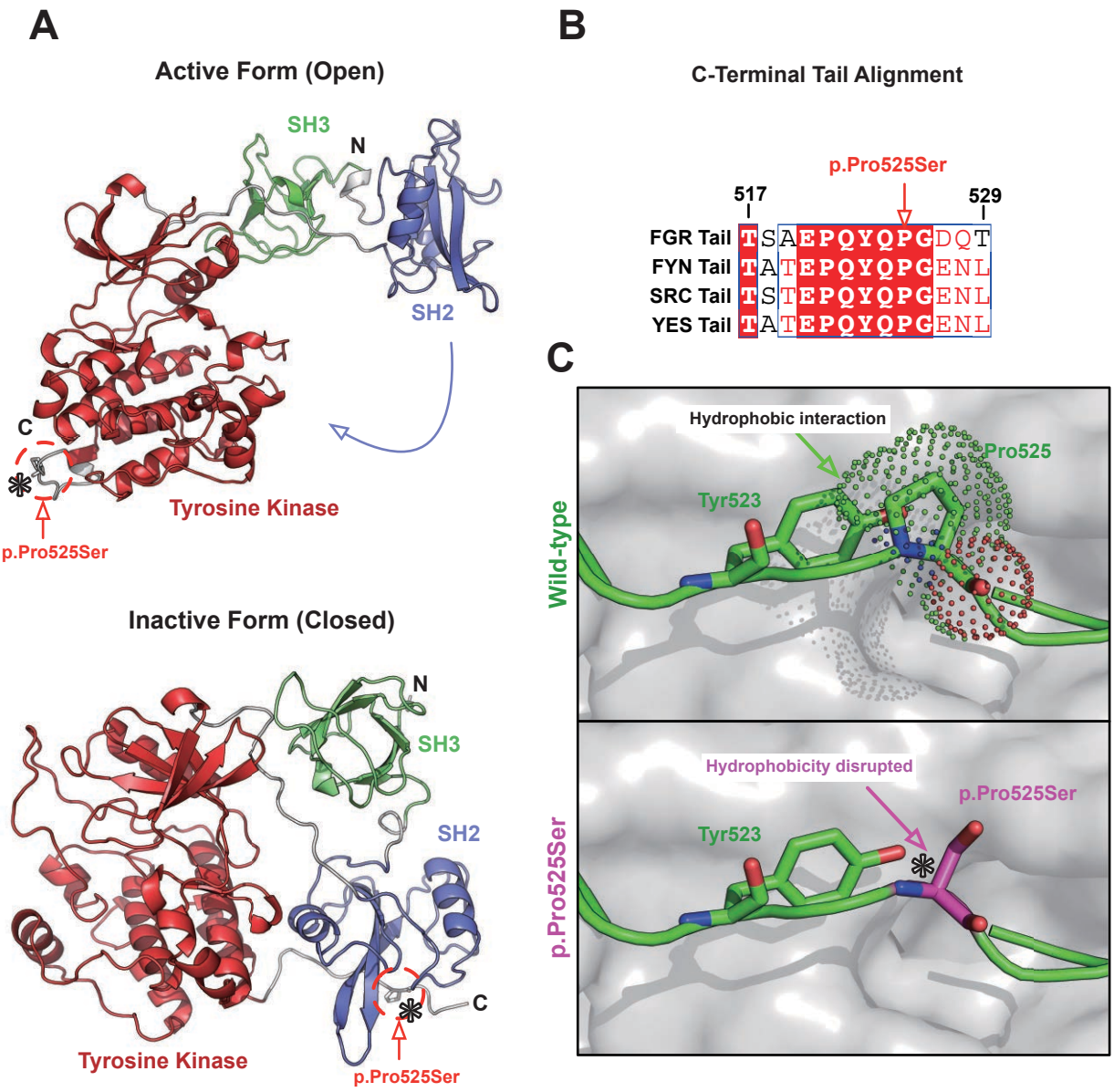

Fig. S6. Predicted mechanism of the human FGR p.Pro525Ser mutation.

(**A**) (Up) Structural model of the active form of FGR modeled off the crystal structure of the human tyrosine kinase C-SRC (PDB: 1Y57). Phosphorylation of Tyr523 by CSK leads to a domain rearrangement that facilitates auto-phosphorylation at Tyr412. The p.Pro525Ser mutation is located at a C-terminal tail that interacts with the SH2 domain. (Down) Structural model of the inactive FGR form modeled off the crystal structure of the human tyrosine kinase C-SRC (PDB: 1FMK). (**B**) Multiple sequence alignment of C-terminal tails from FGR and several other human tyrosine kinases: FYN, SRC, and YES. Multiple sequence alignments were performed using Geneious R9 and visualized in ESPript 3. The p.Pro525 residue is conserved across several tyrosine kinases. (**C**) Close-up of the C-terminal tail of the inactive FGR. (Up) The p.Pro525 residue forms a hydrophobic interaction that binds to the SH2 domain. (Down) The p.Pro525Ser mutation disrupts this hydrophobic interaction and leaves Tyr523 exposed for potential phosphorylation and dephosphorylation. Asterisk indecates amino acid substitution.

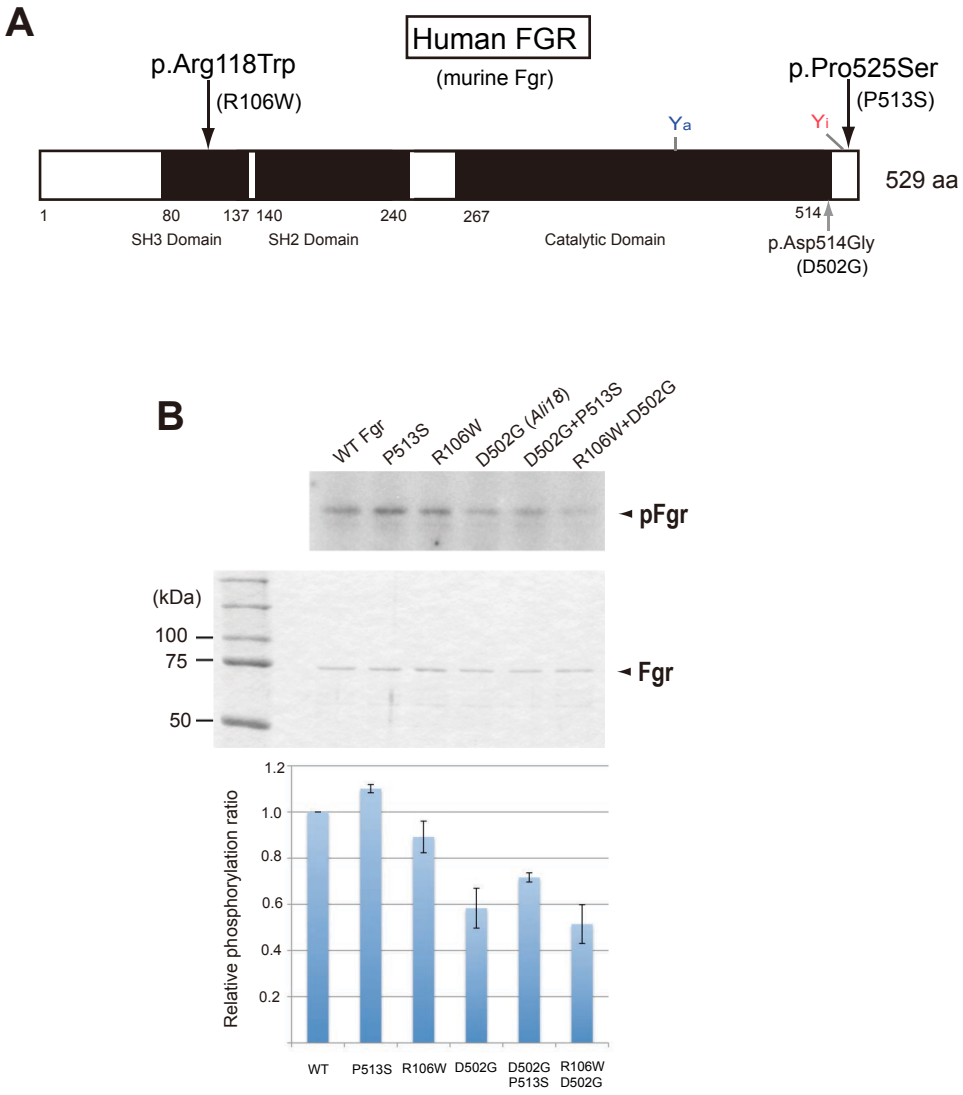

Fig. S7. C-terminal phosphorylation of murin Fgr corresponding to human mutations.(A) Schematic diagram of the amino acid changes caused by human FGR coding mutation found in CRMO. Corresponding murine Fgr mutations were indicated in parentheses. Ya and Yi indicate the autophosphorylation site (412 tyrosine) and the C-terminal regulatory phosphorylation site (523 tyrosine), respectively. (B) Phosphorylation of mutant murine Fgr proteins corresponding human FGR coding mutations by Csk. All Fgr proteins also contain the KD mutation (p.Lys279Met). (top) Phosphorylated Fgr proteins by Csk are shown. The proteins used for kinase assays were fractionated by SDS-PAGE and stained by Coomassie brilliant blue (middle). Experiments are independently triplicated.

Table S1 Genetic mapping of the *Ali18* critical region using in house microsattelite markers

ID	tag	D4Mit12	D4Mit203	D4Neu12	D4Neu6	D4Mit204	D4Mit71	D4Mit339	D4Neu9	D4Mit134	D4Mit54	D4Mit68
10128572	9	B/B	B/B	C/C	C/C	C/C	C/C	C/C	C/C	C/C	C/C	C/C
10135632	69	B/B	B/B	B/B	C/B	C/B	C/B	C/B	C/B	C/B	C/B	C/B
10138700	24	C/B	C/B	C/B	C/B	C/B	C/B	C/B	C/B	B/B	B/B	B/B

B/B: Homozygous for C57BL/6J; C/C: Homozygous for C3HeB/FeJ; C/B: Heterozugous of C3HeB/FeJ and C57BL/6J

Table S2　Summary of Fgr coding variants induced by the CRISPR/Cas9 system in *Ali18* mice

Strain	guide RNA	Nucleotide change	Protein change	Mutation type	Fgr products (predicted)	Fgr haplotype	Generation (genotype)	Inheritance	Swollen paws
#404a	fgRNA1	c.76delC	p.Gln26fs*35	frame shift, nonsense	−	p.Asp502Gly	F1 (*Ali18*/+)	5	0
#404b	fgRNA1	c.75_76insC	p.Gln26fs*4	frame shift, nonsense	−	p.Asp502Gly	F1 (*Ali18*/+)	8	0
#408a	fgRNA1	c.75C>G	p.S25R	missense	+	p.Asp502Gly	F1 (*Ali18*/+)	6	6
#408b	fgRNA1	c.75_76del	p.Ser25fs*4	frame shift, nonsense	−	p.Asp502Gly	F1 (*Ali18*/+)	2	0
#415a	fgRNA1	c.62_81del	p.22fs*2	frame shift, nonsense	−	p.Asp502Gly	F1 (*Ali18*/+)	10	0
#415b	fgRNA1	c.62_88del	p.Gly21_Glu30del	deletion	+	p.Asp502Gly	F1 (*Ali18*/+)	4	4
#416a	fgRNA1	c.76delC	p.Gln26fs*35	frame shift, nonsense	−	p.Asp502Gly	F1 (*Ali18*/+)	4	0
#416b	fgRNA1	c.71_76del	p.Arg24Gln25_26del	missense, deletion	+	p.Asp502Gly	F1 (*Ali18*/+)	1	1
#417a	fgRNA2	c.(−14)_(−3)del	none	SA and 5'UTR deletion	−	p.Asp502Gly	F1 (*Ali18*/+)	6	0
#417b	fgRNA2	c.(−5)_2del	none	5'UTR deletion, synonymus	+	p.Asp502Gly	F1 (*Ali18*/+)	9	4
#418	fgRNA2	c.(−3)_2del	p.Met1del	ATG deletion	−	p.Asp502Gly	F1 (*Ali18*/+)	8	0
#419	fgRNA2	c.(−11)_2del	p.Met1del	SA and ATG deletion	−	p.Asp502Gly	F1 (*Ali18*/+)	5	0

Table S3: All exonic FGR variants found in the 99 CRMO probands

CHR	POS [hg19]	dbSNP ID	Proband	Inheritance	MAF (gnomAD)	REF	ALT	Effect [NM_005248]	Other variants*
1	27939005	rs191541855	A	paternal	0.00006457	A	G	3' UTR	n.d.
1	27939442	rs143850913	Case 2	unknown	0.000354	G	A	P525S	n.d.
1	27941096	rs757288230	B	paternal	0.000008164	TG	T	splice acceptor region §	n.d.
1	27941102	n/a	B	paternal	0	A	T	splice site region	n.d.
1	27942276	rs142998887	C, D, E	paternal/maternal	0.01402	G	A	D254=	n.d.
1	27942362	rs367996753	F, K	paternal	0.001112	G	T	splice site region	FBLIM1
1	27948132	rs2231870	G	maternal	0.003698	G	A	S122=	FBLIM1
1	27948146	rs774209795	Case1	de novo	0.00001218	G	A	R118W	n.d.
1	27952665	rs536321858	H	unknown	0	C	T	5' UTR	n.d.
1	27961658	n/a	I	paternal	0.0001617	G	A	5' UTR	n.d.
1	27961692	rs372572478	J	paternal	0.00006463	G	A	5' UTR	LPIN2

*: Coding variants in CRMO candidate genes which have been characterized. See Table S4 for further information. § : Deletion of 1st G in polypyrimidine tract.

Table S4: Missense variants in CRMO candidate genes found in probands with FGR coding variants.

Gene	CHR	POS [hg19]	dbSNP ID	Protein change	MAF (gnomAD)	Proband	Inheritance
LPIN2	18	2920361	rs201160155	C874F	0.0012	J	maternal
FBLIM1	1	16101332	rs114077715	G311R	0.01954	K	maternal
FBLIM1	1	16101332	rs114077715	G311R	0.01954	G	paternal

Supplementary Table S5: Scoring of FGR proteins by *in silico* predictors

FGR variant	PROVEAN	CADD	SIFT	POLYPHEN2
R118W	-5.015	26.3	D	D
P525S	-2.716	18.2	D	P

References for SI reference citations

1. Toral MA, *et al.* (2017) Structural modeling of a novel SLC38A8 mutation that causes foveal hypoplasia. *Mol Genet Genomic Med* 5(3):202-209.
2. Cox AJ, *et al.* (2017) Recessive coding and regulatory mutations in FBLIM1 underlie the pathogenesis of chronic recurrent multifocal osteomyelitis (CRMO). *PLoS One* 12(3):e0169687.
3. Moshfegh Y, *et al.* (2016) BESTROPHIN1 mutations cause defective chloride conductance in patient stem cell-derived RPE. *Hum Mol Genet* 25(13):2672-2680.
4. Cowan-Jacob SW, *et al.* (2005) The crystal structure of a c-Src complex in an active conformation suggests possible steps in c-Src activation. *Structure* 13(6):861-871.
5. Kaneko T, Li L, & Li SS (2008) The SH3 domain--a family of versatile peptide- and protein-recognition module. *Front Biosci* 13:4938-4952.
6. Waksman G, Shoelson SE, Pant N, Cowburn D, & Kuriyan J (1993) Binding of a high affinity phosphotyrosyl peptide to the Src SH2 domain: crystal structures of the complexed and peptide-free forms. *Cell* 72(5):779-790.
7. Dietrich W, *et al.* (1992) A genetic map of the mouse suitable for typing intraspecific crosses. *Genetics* 131(2):423-447.
8. Dietrich WF, *et al.* (1994) A genetic map of the mouse with 4,006 simple sequence length polymorphisms. *Nat Genet* 7(2 Spec No):220-245.
9. Abe K, Fuchs H, Lisse T, Hans W, & Hrabe de Angelis M (2006) New ENU-induced semidominant mutation, Ali18, causes inflammatory arthritis, dermatitis, and osteoporosis in the mouse. *Mamm Genome* 17(9):915-926.
10. Bagheri-Yarmand R, *et al.* (2001) Etk/Bmx tyrosine kinase activates Pak1 and regulates tumorigenicity of breast cancer cells. *J Biol Chem* 276(31):29403-29409.
11. Cong L, *et al.* (2013) Multiplex genome engineering using CRISPR/Cas systems. *Science* 339(6121):819-823.
12. Xu W, Harrison SC, & Eck MJ (1997) Three-dimensional structure of the tyrosine kinase c-Src. *Nature* 385(6617):595-602.

13. Webb B & Sali A (2016) Comparative Protein Structure Modeling Using MODELLER. *Curr Protoc Protein Sci* 86:2 9 1-2 9 37.
14. Dolinsky TJ, Nielsen JE, McCammon JA, & Baker NA (2004) PDB2PQR: an automated pipeline for the setup of Poisson-Boltzmann electrostatics calculations. *Nucleic Acids Res* 32(Web Server issue):W665-667.
15. Konecny R, Baker NA, & McCammon JA (2012) iAPBS: a programming interface to Adaptive Poisson-Boltzmann Solver (APBS). *Comput Sci Discov* 5(1).
16. Krieger E & Vriend G (2014) YASARA View - molecular graphics for all devices - from smartphones to workstations. *Bioinformatics* 30(20):2981-2982.
17. O'Hare T*, et al.* (2004) Inhibition of wild-type and mutant Bcr-Abl by AP23464, a potent ATP-based oncogenic protein kinase inhibitor: implications for CML. *Blood* 104(8):2532-2539.